Characterizing Nanoplastics-Induced Stress and Its SERS Fingerprint in an Intestinal Membrane Model

Qianyun Zhang and Björn M. Reinhard

Department of Chemistry and The Photonics Center, Boston University, Boston MA 02215,
United States

Key words: nanoplastics, SERS markers, nanotoxicity, metabolomics, hypoxanthine

Epithelium membranes provide important barrier functions, and it is important to understand how nanoparticle (NP) exposure affects their barrier function. In this manuscript, we investigate NP-induced stress in a Caco-2 intestinal epithelial membrane model and its effect on the vibrational spectrum of the extracellular medium that can be sampled and investigated without perturbation of the cells. Monolayers of Caco-2 cells were incubated with 50 nm diameter polystyrene (PS) NPs functionalized with amine or carboxylic acid groups and concentrations of $1\text{x}10^{12}$ – $1\text{x}10^{14}$ PS NPs mL^{-1} for 6 h and 18 h. Reactive oxygen species (ROS) generation, cell viability, and intestinal membrane integrity measurements were performed to detect and quantify PS NP-induced membrane damage under the acute exposure conditions. After identifying conditions that result in NP-induced stress, Surface Enhanced Raman Spectroscopy (SERS) was applied to monitor the composition of the medium in direct contact with the intestinal cells and to detect potential PS NP-induced changes in the cellular metabolism in real time and in a minimally invasive fashion. The analysis of the SERS spectra through artificial intelligence algorithms and chemometric tools revealed concentration-, exposure time-, and surface chemistry-dependent differences in the cellular metabolism in response to PS NPs. The SERS spectral analysis identifies the ring breathing mode of hypoxanthine ($C_4H_4N_4O$), as a spectroscopic marker for the PS NP-induced loss in membrane integrity.

1. Introduction

Plastics is a collective term used for different classes of synthetic polymers that due to their favorable material properties have pervaded all aspects of human life. The annual production of plastics has continuously grown over the last 70 years, reaching a total output of 359 million metric tons in 2018.[1] One inevitable consequence of the anthropogenic use of plastics is its widespread accumulation in the environment. Common synthetic plastics used in packaging and consumer products include polyethylene (PE), polypropylene (PP), polystyrene (PS), polyvinyl chloride (PVC), and polyethylene terephthalate (PET), all of which are not biodegradable. When exposed to the elements, macroscopic objects from these plastics undergo photo-degradation as well as thermo-oxidative and mechanical degradation and gradually fragment into smaller and smaller pieces.[2] Synthetic polymer fragments with dimensions smaller than 5 mm are collectively referred to as microplastics, independent of their exact chemical composition.[3,4] The weathering of plastics does not stop with micrometer-sized particles but continues on sub-micrometer length scales to generate plastic nanoparticles (NPs). Importantly, the environmental mobility, as well as the uptake and fate of these nanoscale particles in animals and humans can differ from larger microplastics of the same chemical composition.[5-7] Due to their large surface-to-volume ratio, NPs show unique interactions with cells and can serve as carriers for adsorbed toxicants.[8-10] However, even materials that are benign in bulk form and free of adsorbed toxicants can show toxicity when formulated as NPs.[11-16]

Lambert *et al.* investigated NP generation from seven macroscopic plastic materials (PE and PP pellets, PP films, PP sheet, PS coffee lids, PET water bottles, polylactic acid (PLA) cups) exposed to accelerated weathering conditions and found that PS and PLA generated the largest amount of NPs.[17] PS NPs can be synthesized with sharp size distributions and defined surface properties, which makes them ideal model systems for characterizing the effect of nanoplastics on cellular systems under defined conditions in this work.[18-23] As the most probable uptake route of PS NPs is *via* ingestion of contaminated food or water, we investigate in this work the interactions of PS NPs with an intestinal membrane model. NPs with diameters < 5 nm can cross the intestinal membrane barrier through paracellular diffusion.[24,25] Larger NPs can cross the intestinal membrane by persorption through degrading epithelial cells[7] or through energy-dependent transcytosis.[26-35] Another concern, in addition to NPs crossing the membrane, is that interactions between NPs and cells perturb cellular functions, damage the intestinal membrane integrity, and compromises its barrier function. Indeed, Thubagere *et al.* observed in an intestinal cell monolayer model that PS NPs uptake can trigger oxidative stress and that the associated NP-induced hydrogen peroxide formation triggers a spread of apoptosis across the entire monolayer.[30] In another study it was shown that 4 h exposure to PS NPs disrupts iron transport across the intestinal epithelium, effectively inhibiting the absorption of the essential nutrient.[36] Although some previous studies have found no indications of PS NP-induced genotoxicity or loss of structural integrity in intestinal membranes models,[37] there is also prior evidence that PS NPs can trigger genotoxicity in epithelial cells and macrophages.[38] Overall, the work performed so far suggests that nanoplastics can have a detrimental effect on the intestinal membrane, but that the effect depends on NP concentration, surface charge, size, and exposure duration. A fundamental understanding of the interactions between nanoplastics and the intestinal membrane as well as the availability of ideally label-free markers of cell stress and membrane damage are key for an accurate risk assessment and to develop effective strategies to mitigate potential detrimental effects.

As interactions between NPs and intestinal cells are complex and depend on a large number of potential variables, *in vitro* intestinal membrane models are frequently used to investigate the effect of plastic NPs on the membrane integrity under defined conditions.[39-42] In these model systems, transepithelial electrical resistance (TEER) measurements facilitate a quantitative monitoring of membrane integrity and permeability.[43-45] Cytotoxicity and cell viability are quantified using MTT and Lactate dehydrogenase (LDH) assays, and the oxidative stress induced by NPs is determined through reactive oxygen species (ROS) measurements.[45-47] Optical and electron microscopies facilitate a characterization of transepithelial NP transport with subcellular spatial resolution.[48-50] NPs also affect the cellular metabolism, and metabolomics is another potentially powerful approach for both detecting and characterizing cellular responses to NPs at a molecular level.[51-53] NP-induced differences in the cell metabolism cause changes in the composition of cells as well as the extracellular medium due to variations in the nature and quantity of the molecules uptaken by and released from the cells.[54] Although metabolomics is traditionally performed with mass spectroscopy, Raman spectroscopy, in particular surface enhanced Raman spectroscopy (SERS), has shown promise for the metabolic profiling of the cellular activity of bacterial cells and human cancer cells,[55-60] as well as for the detection of biomarkers in serum.[55, 61,62] SERS is a vibrational spectroscopy that provides unique opportunities for signal amplification in aqueous media as water has low Raman cross-sections while the signal from Raman-active molecular vibrational modes in analytes can be enhanced by multiple orders of magnitude due to an electromagnetic enhancement effect in the vicinity of nanostructured noble metal surfaces.[63-67] This amplification of molecule-specific vibrational information facilitates a sensitive detection and identification of metabolites rapidly without the need for elaborate sample preparation or enrichment. In this work, we exposed an *in vitro* intestinal cell membrane model with PS NPs in a concentration range that warrants NP-induced cell stress and combined TEER, ROS and cell viability measurements with SERS measurements to validate, characterize and identify nanoplastics-induced changes in the vibrational spectrum of the extracellular medium under conditions of increased intestinal membrane permeability.

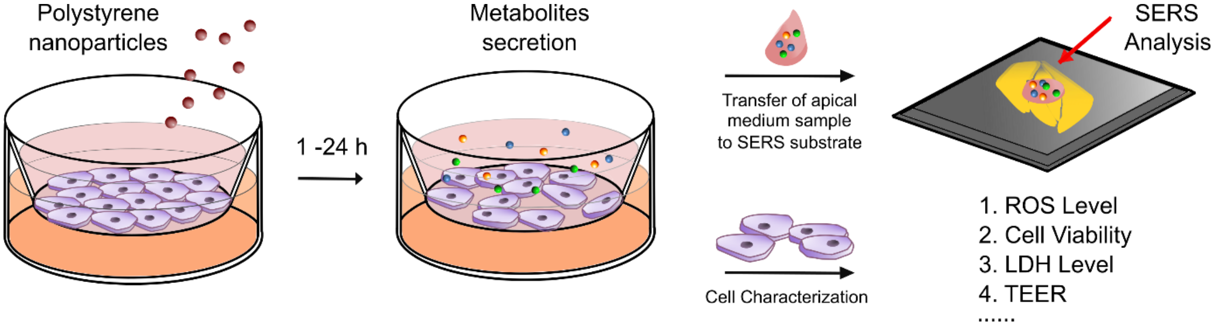

Figure 1. Schematic drawing of the experimental setup. Metabolites are shown as colorful beads.

Table 1. Nanoplastic particles characterization (t=0h, n=10)

Particle	D_H in MQ water [nm]	D_H in growth medium [nm]	ζ in 10mM NaCl [mV]	ζ in growth medium [mV]
NH_2-PS	57±5	96±12	48.7±2.1	-6.1±1.2
COOH-PS	64±8	89±13	-50.7±2.3	-9.6±0.7

2. Results and Discussion

The size and surface charge of nanoplastics generated in the environment is determined by the weathering process and can vary depending on the specific conditions. We used colloidal PS NPs with amine (NH_2-PS) or carboxylate (COOH-PS) surface ligands as model system in this work to investigate the interactions between PS NPs and cells under well-defined conditions. The hydrodynamic diameter and zeta potential of the NPs in water and growth medium are summarized in **Table 1**. In water, the hydrodynamic diameter is 57 ± 5 nm for NH_2-PS, and 64 ± 8 nm for COOH-PS, and the zeta potential (ζ) of NH_2-PS is 48.7 ± 2.1 mV compared to -50.7 ± 2.3 mV of

COOH-PS. In growth medium, the initial hydrodynamic diameter (D_H) increases to 96 ± 12 nm for NH_2-PS and 89 ± 13 nm for COOH-PS, and we measured a zeta potential of -6.1 ± 1.2 mV for NH_2-PS and -9.6 ± 0.7 mV for COOH-PS. We attribute the nearly identical zeta potentials for both NH_2-PS and COOH-PS and its low absolute value in growth medium that is rich in proteins and other biopolymers to non-specific protein adsorption, *i.e.* corona formation.[68-70] The hydrodynamic diameter of both NH_2-PS and COOH-PS in growth medium gradually increases as function of time and converges against approximately 350 nm in the case of NH_2-PS and 150 nm in the case of COOH-PS after ~6 h (**Figure S1a**). SEM images (**Figure S1b**) reveal that this additional increase in the hydrodynamic diameter is due to some self-association of the PS-NPs. The different NP stabilities (*i.e.* hydrodynamic diameters) point to differences in the composition and structure of the corona formed around NH_2-PS and COOH-PS.

Caco-2 cells are human colon carcinoma cells that grow into a monolayer on permeable membranes. The cells can be induced to differentiate into mature absorptive enterocytes with well-developed microvilli, tight apical junctions, and a polarized distribution of membrane components.[39-42,71-74] Due to the resemblance of Caco-2 cells with intestinal enterocytes, differentiated Caco-2 cell monolayers are a common model system to study the transepithelial membrane transport of various NPs, including polymeric[71-73] and plastic NPs[33-38], at a fraction of the cost and without the ethical implications of a small animal experiment. In this work, NH_2-PS and COOH-PS were incubated with differentiated monolayers of Caco-2 cells for 6 h or 18 h, which are typical incubation times for mechanistic barrier studies of Caco-2 cells[34-37,75] Subsequently, the effect of the PS NPs on the intestinal membrane health was evaluated, and a SERS analysis of the medium was performed to identify changes in the cellular metabolism. **Figure 1** summarizes the experimental approach of this work.

2.1 NH_2-PS and COOH-PS Uptake by Caco-2 Cells

Throughout this manuscript, we used PS NPs that contained fluorescent dyes embedded in their core as these are easily tractable through fluorescence microscopy. We validated that fluorescence dye release on the time scale of our experiments (up to 18 h) is negligible (**Table S1**). Confocal microscopy scans confirmed that both NH_2-PS and COOH-PS bind to and get internalized by Caco-2 cells (**Figure 2a**). The NPs were incubated with the cells for 6 h before the number of uptaken NPs was determined by measuring their fluorescence signal. The effect of PS NPs on the intestinal membrane is expected to be concentration and time dependent. Concentrations of up to 1.5×10^{12} NPs mL^{-1} of PS NPs were shown to have negligible effect on membrane integrity within an exposure time of 24h.[47] In this work significantly higher PS NPs concentrations in the range of 1×10^{12} – 1×10^{14} NPs mL^{-1} were investigated to ensure conditions that induce a measurable damage to the membrane within the limited observation time of our experiments (18 h). The chosen NP concentrations emulate oral administrations of 10 mg kg^{-1} and 1000 mg kg^{-1} of 50 nm PS NPs to a 70 kg human (assuming the total surface area of the human small intestine is 2×10^6 cm^2 [76] and the presence of microvilli increases the surface area by a factor of 20[77]). In this concentration range, uptake was well described by a Hill-Langmuir like expression of the form $NP_{assoc.} = NP_{max}\frac{[NP]}{K+[NP]}$ where $NP_{assoc.}$ is the number of NPs per cell, NP_{max} is the maximum number of NPs uptaken by the cells, [NP] is the input concentration of NPs, and K is a NP-specific parameter that describes binding and uptake in differentiated Caco-2 cell monolayers (**Figure 2b, 2c**). A smaller value of K indicates a higher binding affinity and increased uptake. Our fits yielded $K = 2.6 \times 10^{12}$ NPs mL^{-1} for NH_2-PS compared to 2.6×10^{13} NPs mL^{-1} for COOH-PS. The higher uptake of NH_2-PS at low to medium input concentrations indicates a higher binding affinity to Caco-2 cells for NH_2-PS than for COOH-PS.

As the zeta potentials of NH_2-PS and COOH-PS under cell culture conditions were nearly identical in our work (**Table 1**), we attribute the differences in binding and uptake to differences and the corona assembled around NH_2-PS and COOH-PS. Positively charged NPs have a higher affinity for serum proteins,[78] so that the surface properties of NH_2-PS and COOH-PS can result in the formation of coronas with different composition in biological media. [79] It was shown previously that NH_2-PS contain a higher number of apolipoproteins in the corona than COOH-PS, which can have a direct effect on NP uptake. [69, 80, 81] The difference in particle size due to self-association observed for longer incubation times (**Figure S1**) may also contribute to differences in the uptake between NH_2-PS and COOH-PS.

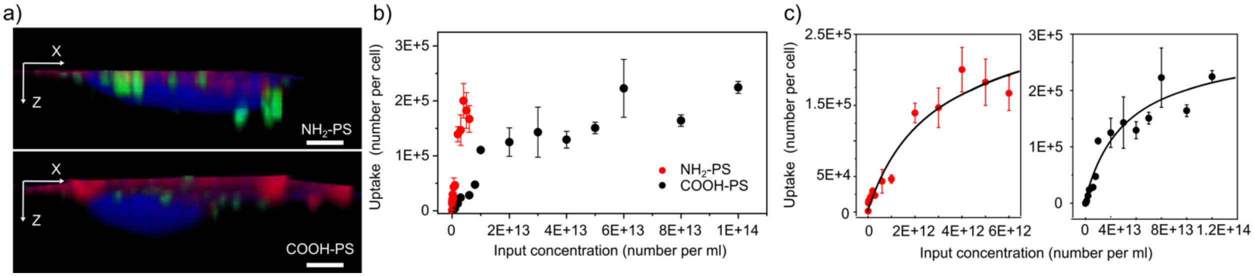

Figure 2: a) Cross-sectional confocal 3D images (xz plane) of a monolayer of Caco-2 cells show NH_2-PS and COOH-PS uptake (green) into the cells after 6 h NP addition. Cell junctions at the apical surface were stained with ZO-1 antibody (red) (top), and nuclei were stained with Hoechst 33324 (blue) (bottom). Scale bar: 1 µm b) NH_2-PS (red) and COOH-PS (black) uptake by a monolayer of Caco-2 cells as function of NP input concentration, measured 6 h after NP addition. c) Fits to the concentration-dependent uptake for NH_2-PS (left) and COOH-PS (right). The data in b) and c) represent averages of n = 20 independent experiments.

In the remainder of this manuscript, we used NH_2-PS input concentrations of *C1* (NH_2-PS) = $1x10^{12}$ NPs mL^{-1} and *C2* (NH_2-PS) = $6x10^{12}$ NPs mL^{-1}, and COOH-PS input concentrations of *C1* (COOH-PS) = $6x10^{12}$ and *C2* (COOH-PS) = $1x10^{14}$ NPs mL^{-1}. The input concentrations were chosen to yield comparable uptake of NH_2-PS and COOH-PS: 0.46 $x10^5$ and 0.28 $x10^5$ NPs $cell^{-1}$

for *C1;* $2.2\text{x}10^5$ and $1.7\ \text{x}10^5$ NPs cell^{-1} for *C2* (**Figure S2**). Two sets of NH_2-PS and COOH-PS input concentrations that yield nearly identical uptake levels in Caco-2 facilitated a systematic comparison of the effects of NH_2-PS and COOH-PS on Caco-2 cells and the intestinal membrane model as a whole.

2.2 Effect of PS NPs on ROS Levels and Cell Viability

Reactive oxygen species (ROS) generation is a cellular stress response to the uptake of non-biodegradable NPs, including nanoplastics,[82-83] and NP-induced increases in ROS can result in a loss of Caco-2 membrane integrity.[30] We quantified the ROS levels in differentiated Caco-2 monolayers incubated with NH_2-PS and COOH-PS and concentrations *C1* and *C2* at four time points (1 h, 3 h, 6 h, 18 h) after PS NPs addition (**Figure 3a**). *C1* achieves increased ROS levels for both NH_2-PS and COOH-PS at 6 h. In case of *C2*, significantly increased ROS levels are detected at 1 h, 3 h, 6 h for NH_2-PS and at 3 h and 6 h for COOH-PS. For both flavors of NPs, the ROS levels increase with NP input concentration and peak at around 3 h to 6 h.

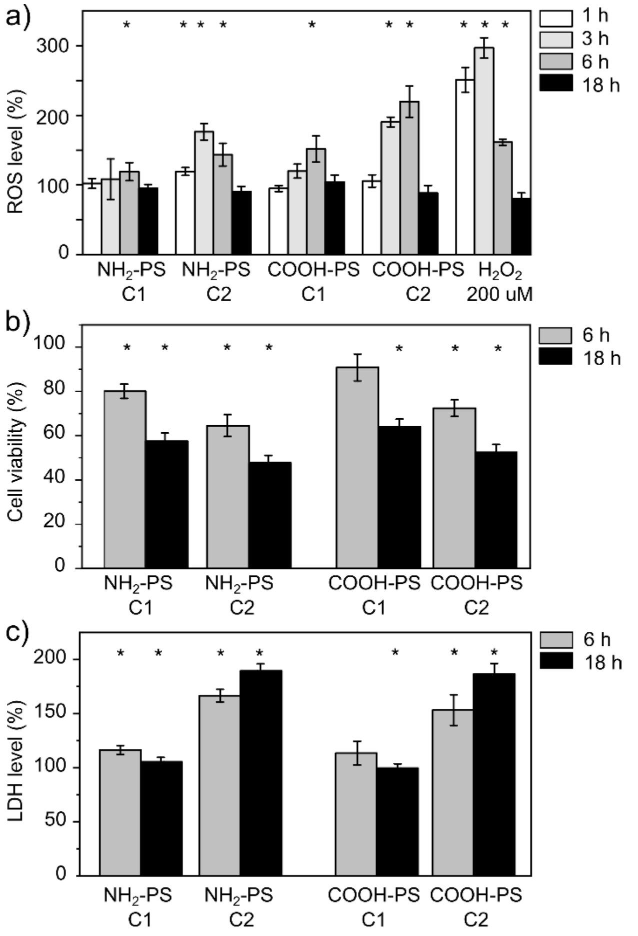

Figure 3: Characterization of a) ROS, b) cell viability, and c) LDH levels after incubation of monolayers of Caco-2 cell with NH_2-PS (*C1*: 1×10^{12} NPs mL^{-1} and *C2*: 6×10^{12} NPs mL^{-1}) and COOH-PS (*C1*: 6×10^{12} NPs mL^{-1} and *C2*: 1×10^{14} NPs mL^{-1}) for 6 h and 18 h. Results were normalized with the no treatment controls and are given in % (100% = control). H_2O_2 was included in a) as positive control. The data in a)-c) represent an average of n = 20 independent experiments. * indicates a significant difference at the $p < 0.05$ level.

The effect of NH_2-PS and COOH-PS on cell viability was characterized through microculture tetrazolium (MTT) assays (**Figure 3b**) performed 6 h and 18 h after NP addition. In the case of NH_2-PS, a significant reduction in cell viability relative to the no treatment control was detected

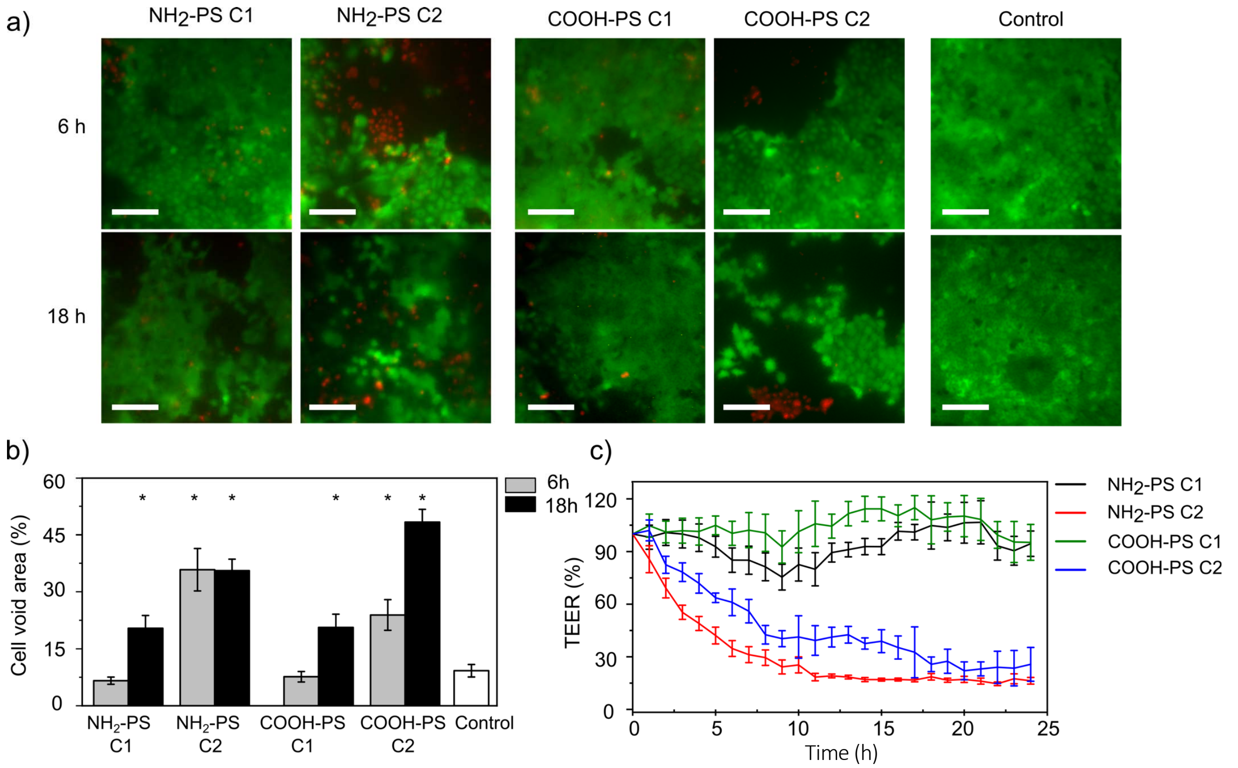

Figure 4: a) Fluorescence images of differentiated Caco-2 cell monolayers treated with NH_2-PS (*C1*: $1x10^{12}$ NPs mL^{-1} and *C2*: $6x10^{12}$ NPs mL^{-1}) and COOH-PS (*C1*: $6x10^{12}$ NPs mL^{-1} and *C2*: $1x10^{14}$ NPs mL^{-1}) for 6 h and 18 h and treated with a live (green) and dead (red) stain. Scale bar: 50 µm. b) Quantification of the membrane areas void of cells (in %). c) TEER for monolayers of differentiated Caco-2 cells as function of time when incubated with high and low concentrations of NH2-PS and COOH-PS. Results were normalized with the control group. The data in b), c) represent an average of n=10 independent experiments. * indicates a significant difference at the $p<0.05$ level.

for concentrations *C1* and *C2* at both time points. COOH-PS show a similar behavior with the exception that the MTT value for concentration *C1* at 6 h is not yet significantly reduced relative to the no treatment control. For both flavors of NPs the cell viability decreased with input concentration and exposure time. We applied lactate dehydrogenase (LDH) assays as a second strategy to characterize the cytotoxicity of NH_2-PS and COOH-PS at 6 h and 18 h after addition of the PS NPs (**Figure 3c**). For concentration *C1*, NH_2-PS and COOH-PS, show only modest differences in LDH levels relative to the no-treatment control, but for concentration *C2,* a strong increase of LDH levels is detected at 6 h and 18 h for NH_2-PS and COOH-PS. Both MTT and LDH assays confirm that NH_2-PS and COOH-PS can reduce the viability of Caco-2 cells and that the effect increases with NP input concentration and incubation time. Overall, we find that NH_2-PS and COOH-PS have similar effects on the cell viability for input concentrations that yield similar NP uptake.

To test for a potential PS-NP induced damage to the Caco-2 cell monolayer, we mapped dead cells with a live and dead stain through fluorescence microscopy (**Figure 4a**). We performed these experiments with both NH_2-PS and COOH-PS and concentrations *C1* and *C2* 6 h and 18 h after addition of PS NPs. Images of differentiated Caco-2 cell monolayers not exposed to NPs were included as controls. In the absence of PS NPs and for PS NPs concentration *C1* the fluorescence images show an intact membrane of living (green) cells with only a few dead (red) cells whose frequency is higher for 18 h than for 6 h. The number of dead cells increases for NH_2-PS and COOH-PS with concentration *C2* and large areas void of cells emerge, presumably because dead cells have detached from the membrane support in these areas. **Figure 4b** summarizes the area in % in the cell monolayer that is void of cells. The plot confirms that the "holes" in the cell monolayer increase in size with time and concentration of NPs. One notable exception is NH_2-PS at high concentrations, for which essentially identical areas void of cells were detected at 6 h and 18 h.

The detachment of dead cells from the membrane support accounts for the holes in the Caco-2 cell monolayers observed in **Figure 4b** and also provides an explanation for the steep drop in the ROS levels observed for NP-treated cells between 6 h and 18 h in **Figure 3a**. Dead and detached cells are removed during the wash step, and a lower number of cells with increased ROS levels after 18 h of NP treatment result in ROS levels that are comparable to those of a higher number of healthy control cells that generate less ROS per cell. Indeed, if we normalized the ROS levels by the number of cells on the substrate, we found significantly enhanced ROS levels relative to the no treatment controls for all PS NPs conditions at t = 18 h (**Figure S3**).

2.3 Characterizing the Effect of PS NPs on Caco-2 Membrane Integrity

We measured the TEER of monolayers of differentiated Caco-2 cells incubated with NH_2-PS or COOH-PS with concentration *C1* or *C2* every hour for a total of 24 h (**Figure 4c**). All TEER values are normalized by the no treatment control for the same time point. For NH_2-PS with an input concentration of *C1*, the TEER remains constant for the first 2 h before it transiently decreases by approximately 30%. After approximately 10 h, the TEER starts to increase again and eventually converges against the starting value prior to NP exposure. If the NH_2-PS concentration is increased to *C2*, a fast, continuous and non-reversible drop of the TEER value by nearly 80% of its initial value is observed within the first 10 h. In the case of COOH-PS, the TEER does not decrease over the entire observation time for *C1*, but an increase of the input concentration to *C2* results in a rapid and continuous decrease in TEER of similar magnitude as observed for NH_2-PS. The strong decrease in TEER for concentration *C2* of NH_2-PS and COOH-PS indicates an increased permeability of the cell monolayer and is consistent with the substantial detachment of dead cells from the membrane observed for these conditions in the live/dead staining experiments in **Figure 4a**.

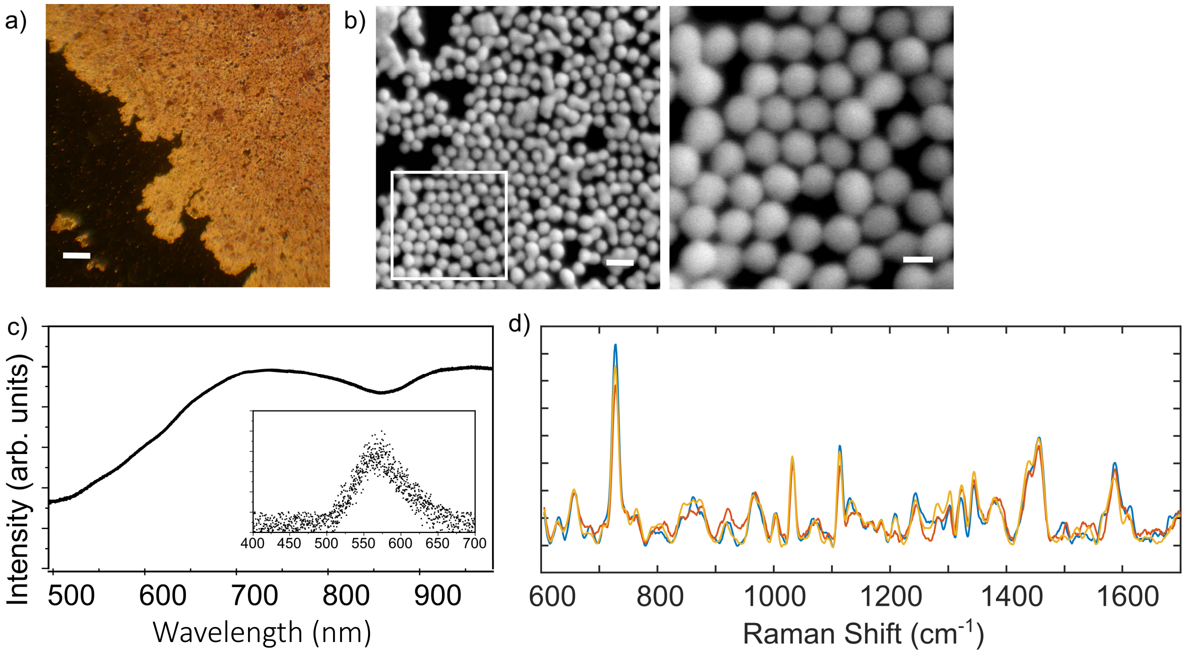

Figure 5: a) Optical image of a gold NP (80 nm) monolayer used as SERS substrate in this work. Scale bar: 50 µm. b) SEM images of a section of the gold NP film (left, scale bar: 150 nm), and zoom-in view (right, scale bar: 50 nm. c) Scattering spectrum of SERS substrates. Inset: Scattering spectrum of gold colloid nanoparticles. d) Three presentative SERS spectra of medium collected from Caco-2 cells after 18 h of incubation with NH_2-NP (*C2*: $6x10^{12}$ NPs mL^{-1}).

2.4 Vibrational Characterization of the Growth Medium of Caco-2 Cell Monolayers through SERS

After identifying PS NPs conditions that result in a decrease of the Caco-2 cell monolayer integrity, we apply in this section SERS for a vibrational characterization of the medium in which the Caco-2 cells are cultured to screen for metabolomic changes induced by the PS NPs. The underlying hypothesis is that PS NP-induced changes in the cellular metabolism lead to changes in the extracellular medium through changes in the cellular uptake of nutrients from the medium or release of metabolites into the medium, and that these changes can be sensitively detected with no special sample preparation through SERS. The electromagnetic amplification of the Raman signal in SERS depends on the fourth power of the electric (E-)field (~E^4). SERS spectra are consequently typically recorded on nanostructured noble metal surfaces that provide strong local E-fields through excitation of Localized Surface Plasmon Resonances (LSPRs). [63-67,85] In this work, we prepared monolayers of gold NPs with a diameter of 78±1 nm by the Langmuir-Blodgett (LB) technique and transferred them onto a glass coverslip as SERS substrates (see Methods). An optical darkfield image of a substrate is shown in **Figure 5a**. SEM micrographs show a layer of closely packed NPs with nanoscale crevices and junctions between individual NPs (**Figure 5b**). Under resonant excitation, these nanogap structures form electromagnetic "hot-spots" that provide strong E-fields to amplify the Raman signal of molecules localized to these gaps.[86] The scattering spectrum of the gold NP film (**Figure 5c**) shows a broad plasmon band that is strongly broadened and red-shifted when compared with the colloidal gold NP building blocks (inset in **Figure 5c**). The strong spectral shift of the plasmon confirms strong electromagnetic coupling between the NPs in the film. All SERS measurements reported in this study were performed with a laser excitation at 785 nm as it overlaps with the plasmon resonance of the gold NP film and because the fluorescence background is generally low in this wavelength range.

We recorded SERS spectra of growth medium collected from the apical compartment of the Caco-2 monolayers incubated with NH_2-PS and COOH-PS with concentration *C1* and *C2* 6 h and 18 h after NP addition. At both time points we also measured SERS spectra of the growth medium collected from cells not incubated with NPs as well as of NH_2-PS and COOH-PS incubated in medium without cells as controls. SERS measurements for each condition were performed with 5 independent experiments: each on a new SERS substrate and from a new Caco-2 cell culture. Within each independent SERS measurement, five spectra were collected from different locations on one substrate. **Figure 5d** shows three representative spectra of medium samples collected from NH_2-PS (*C2*: 6×10^{12} NPs mL^{-1}) treated cells after 18 h of incubation. A close inspection of the three spectra recorded under identical conditions reveals some variability between the spectra. For some peaks the relative intensities differ between the spectra, while other peaks are only detectable in selected spectra. Due to the strong Raman signal intensity enhancement provided by electromagnetic hot-spots, the SERS signal recorded at a particular location of the SERS substrate depends on the chemical composition of the hot-spots. The biological medium investigated in this work has a complex composition, containing amino acids, lipids, carbohydrates, nucleic acids and other nutrients, as well as metabolites released from the cells. This chemical complexity can result in differences in the composition of the hot-spots and, thus, the recorded spectra.[87-91] In addition to the compositional heterogeneity, the hot-spots also have a morphological heterogeneity that results in differences in the E-field enhancement between individual hot-spots. [65] These two effects in addition to differences in the orientation of analyte molecules in the hot-spots are sources of variability in the recorded SERS spectra.[56]

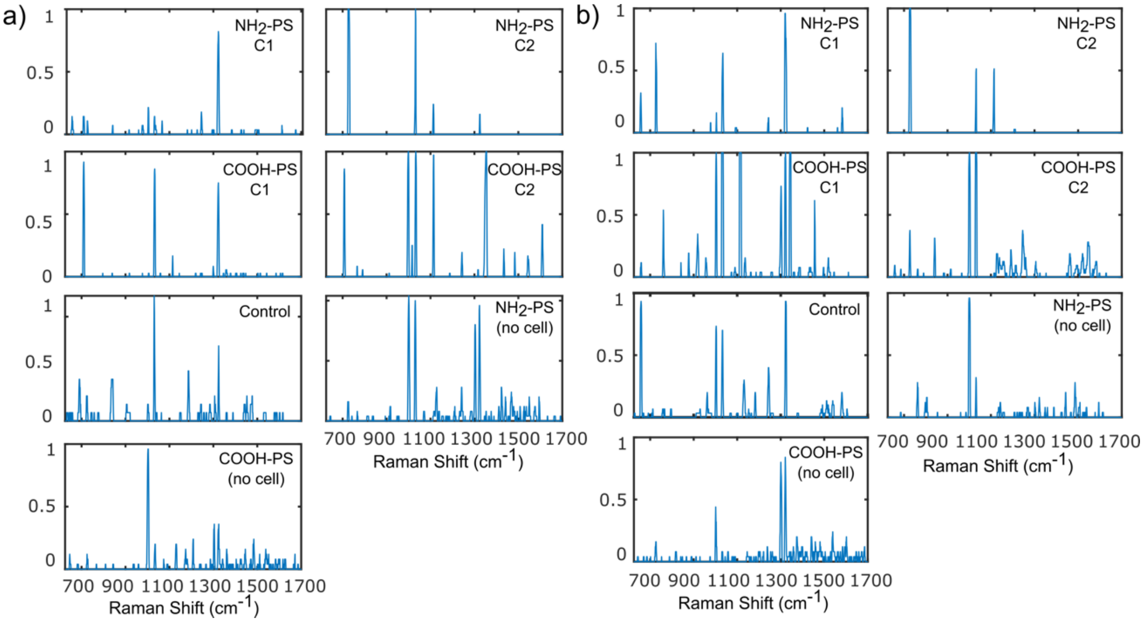

Figure 6: a) Histograms of the second derivative spectra collected from media incubated with NH_2-PS (*C1*: 1x10^{12} NPsmL^{-1} and *C2*: 6x10^{12} NPs mL^{-1}) and COOH-PS (*C1*: 6x10^{12} NPs mL^{-1} and *C2*: 1x10^{14} NPs mL^{-1}), and no particles (cell control) for 6 h. The spectra for NH_2-PS (6x10^{12}

NPs mL^{-1}) and COOH-PS (1×10^{14} NPs mL^{-1}) incubated in medium with cells are also included. b) Same data for 18 h.

Given the heterogeneity of the SERS spectra, each experimental condition is best described by an ensemble of spectra, and a systematic comparison between experimental conditions should be based on the analysis of the ensembles.[92] To obtain an overview of the spectral ensembles of this work, we calculated the second derivative spectra and determined the maxima, defined as all features with a negative second derivative whose absolute value was at least 2.5 standard deviations higher than the noise in each spectrum. The second derivatives spectra were calculated with the PLS toolbox (Eigenvector Research) in MatLab. The fraction of spectra containing the identified maxima provide a measure of the relative frequency of that feature in the ensemble. The histograms of the peak positions obtained in this way are summarized in **Figure 6** for the different experimental conditions recorded 6 h or 18 h after addition of the NPs. A visual inspection of the histograms suggests differences in the spectra recorded for PS NPs treated cells and no treatment controls as well as between the different NP conditions. To corroborate this hypothesis and to identify the spectral features that are responsible for the differences, we next applied artificial intelligence and chemometric data analysis strategies. T-distributed stochastic neighbor embedding (t-SNE) is a machine learning algorithm for dimensionality reduction and visualization.[93] Each point in the t-SNE plot in **Figure 7** represents a single SERS measurement. At 6 h (**Figure 7a**), the spectra recorded for NH_2-PS and COOH-PS with concentration *C2* separate clearly from each other and the no treatment and NP controls. The no treatment and NP controls also cluster at 6 h, but the individual clusters are less well defined and separated. With increasing time, the clustering overall improves and the individual clusters become more distinct at 18 h

(**Figure 7b**). The clustering of the spectra in the t-SNE plots confirms that the spectra of one condition share similarities with each other and systematic differences with other conditions.

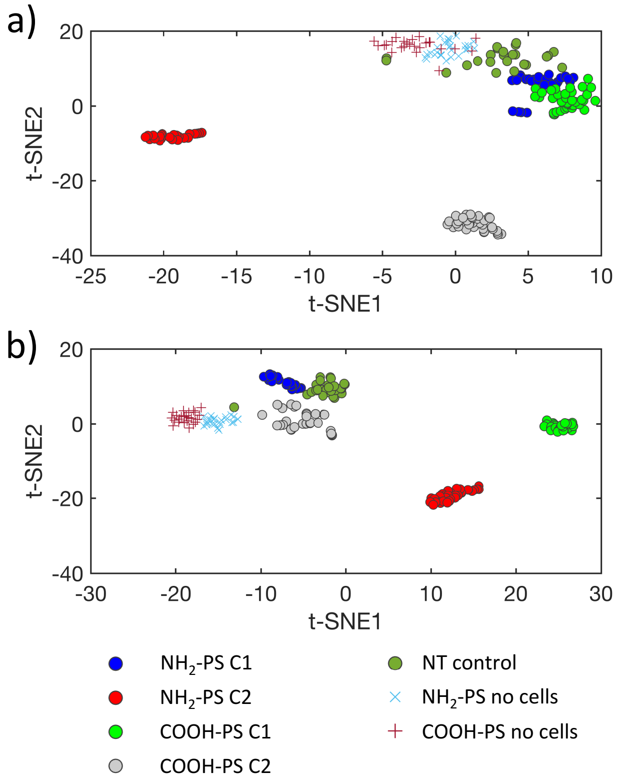

Figure 7: t-Distributed stochastic neighbor embedding (t-SNE) analysis of the second derivative SERS spectra of the medium collected from Caco-2 cells incubated with COOH-PS (*C1*: 6x10^{12} NPs mL^{-1}, *C2*: 1x10^{14} NPs mL^{-1}), NH_2-PS (*C1*: 1x10^{12} NPs mL^{-1}, *C2*: 6x10^{12} NPs mL^{-1}), no particles cell controls (NT control), and NH_2-PS and COOH-PS (NPs incubated in medium without cells) collected a) 6 h and b) 18 h after NP addition.

To further characterize the degree of similarity and dissimilarity between the different conditions, as well as to identify the spectral features that are responsible for the differences, we next performed Principal Component Analysis (PCA)[94] and principal component discriminant analysis (PCA-LDA)[95]. PCA reduces the number of variables of a data set by projecting the data onto a lower dimensional space spanned by so-called principal components (PCs) that are weighed linear combinations of the original variables. In the reduced presentation, the individual spectra are defined by “scores” for the individual PCs. In PCA-LDA, linear discriminant analysis (LDA) is subsequently applied on the reduced data presentation to maximize the separation between the individual groups of observations, yielding a set of scores on a new set of linear discriminant (LD) axes. Importantly, the PCs and LDs that can separate the SERS spectra of different groups contain information about the spectral features that are responsible for the systematic differences. PCA of the second derivative spectra was performed using PCA as integrated in Matlab. The first 20 PCs were used as input for an LDA analysis that was performed with a home written code based on Chen and Hsu[96] in Matlab (see Methods).

Figure 8a,b shows PCA score plots in the PC2-4 space for the spectra recorded (a) 6 h and (b) 18 h after PS NPs addition. After 6 h, the spectra of COOH-PS and NH_2-PS with concentration *C2* are well separated from each other and all other conditions, which implies i.) that these two conditions have a particular strong effect on the cells and ii.) that the cellular responses to these two NPs with different surface chemistries differ. The spectra obtained for COOH-PS and NH_2-PS with concentration *C1* form clusters that lie close together. Likewise, the clusters of the no treatment control and of COOH-PS and NH_2-PS incubated with growth medium in the absence of cells also overlap, albeit in a separate region of the PC2-4 space than the spectra collected from cells incubated with PS NPs. Based on this clustering pattern, we can conclude that both flavors of PS NPs induce detectable cellular changes already after 6 h even for *C1*, but that the spectral differences between COOH-PS and NH_2-PS are still modest. After 18 h, the separation between

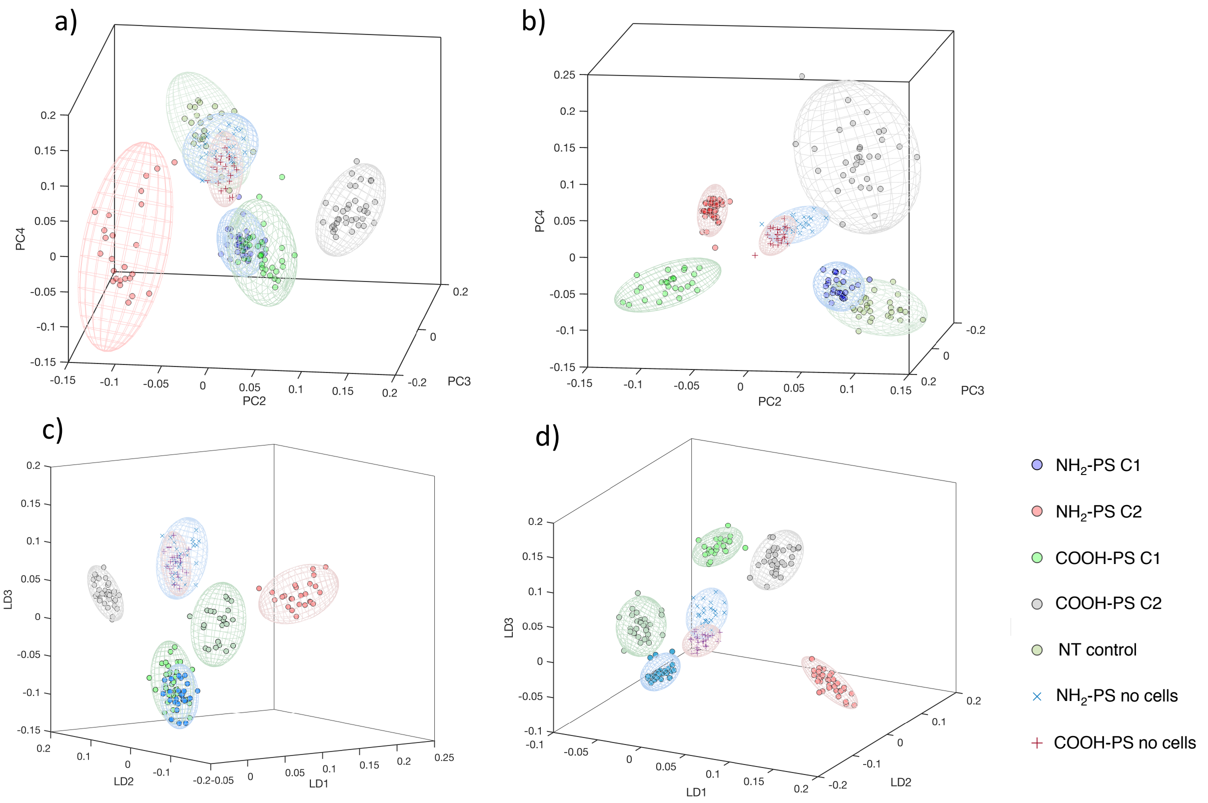

Figure 8: a-b) PCA score plots (PC2-4 space) of the SERS spectra of medium collected from Caco-2 cells incubated with COOH-PS (*C1*: 6x10^{12} NPs mL^{-1}, *C2*: 1x10^{14} NPs mL^{-1}), NH_2-PS (*C1*: 1x10^{12} NPs mL^{-1}, *C2*: 6x10^{12} NPs mL^{-1}), no particles cell controls (NT control), and NH_2-PS and COOH-PS (NPs incubated in medium without cells) collected a) 6 h and b) 18 h after NP addition. c-d) PCA-LDA score plots (LD1-3 space) of the SERS spectra medium collected from Caco-2 cells incubated with COOH-PS (*C1*: 6x10^{12} NPs mL^{-1}, *C2*: 1x10^{14} NPs mL^{-1}), NH_2-PS (*C1*: 1x10^{12} NPs mL^{-1}, *C2*: 6x10^{12} NPs mL^{-1}), no particles cell controls (NT control), and NH_2-PS and COOH-PS (NPs incubated in medium without cells) collected after c) 6 h and d) 18 h. Shaded regions in a)-d) represent 90% confidence intervals.

the individual groups has overall improved, but the clusters NH_2-PS with *C1* and the no treatment control still overlap in the PCA score plot as do the clusters for the NH_2-PS and COOH-PS no cells controls. PCA-LDA yields overall similar trends as PCA but with further improved separation between the clusters in the LD1-3 space (**Figure 8c, d**). For the data set recorded after 6 h, PCA-LDA achieves a clear separation of both concentrations of COOH-PS and NH_2-PS from the no treatment and NP controls. For the data recorded after 18 h, PCA-LDA achieves more compact clusters and better separations between the clusters when compared with PCA performed at the same time point. At 18 h, the only clusters whose 90% confidence intervals still overlap in the LD1-3 space are the COOH-PS and NH_2-PS no cell controls, which are conditions for which no change in the growth medium is expected.

Overall, the multivariate data analysis is consistent with the t-SNE analysis and confirms that both COOH-PS and NH_2-PS induce changes in the composition of the growth medium and that these changes increase with the concentration of the NPs and incubation time. Intriguingly, although COOH-PS and NH_2-PS were compared under conditions that yield comparable uptake, the SERS spectra of the medium collected from cells treated with these particles can be distinguished not only from the no treatment control but also from each other. The spectra of all PS NPs treated cells separate from the no treatment controls along LD1 in **Figure 8d**, while the spectra of COOH-PS and NH_2-PS separate along LD3. This finding suggests that all PS NPs elicit a significant cellular response, but it also implies that the responses to COOH-PS and NH_2-PS are not completely identical. Information about the spectral features that are responsible for separating the different conditions in PCA or PCA-LDA score plots are contained in the loading spectra. These spectra plot the contribution of each wavenumber to a PC or LD. We focus here on the analysis of LDs as PCA-LDA provides the clearest separation between the different experimental conditions. The loading spectra for LD1-3 after 6 h and 18 h are plotted in **Figure 9a, 9b**. The spectral features that have prominent contributions in multiple loading spectra include peaks at (+/- 3 cm^{-1}) 728 cm^{-1} ($LD1^{6h}$, $LD2^{6h}$, $LD1^{18h}$), 1002 cm^{-1} ($LD3^{6h}$, $LD2^{18h}$, $LD3^{18h}$),1032 cm^{-1} ($LD1^{6h}$, $LD2^{6h}$, $LD1^{18h}$, $LD2^{18h}$, $LD3^{18h}$), 1115 cm^{-1} ($LD2^{6h}$, $LD1^{18h}$, $LD2^{18h}$, $LD3^{18h}$), 1320 cm^{-1} ($LD1^{6}$, $LD3^{6h}$, $LD2^{18h}$), 1343 cm^{-1} ($LD1^{18h}$, $LD2^{18h}$), and 1457 cm^{-1} ($LD2^{6h}$, $LD1^{18h}$). In LDx^{y}, x specifies the number of the LD and y the time of sampling. The detailed peak assignments of all loading spectra are summarized in **Table S2**. The prominent feature at 728 cm^{-1} in LD1, which separates the spectra

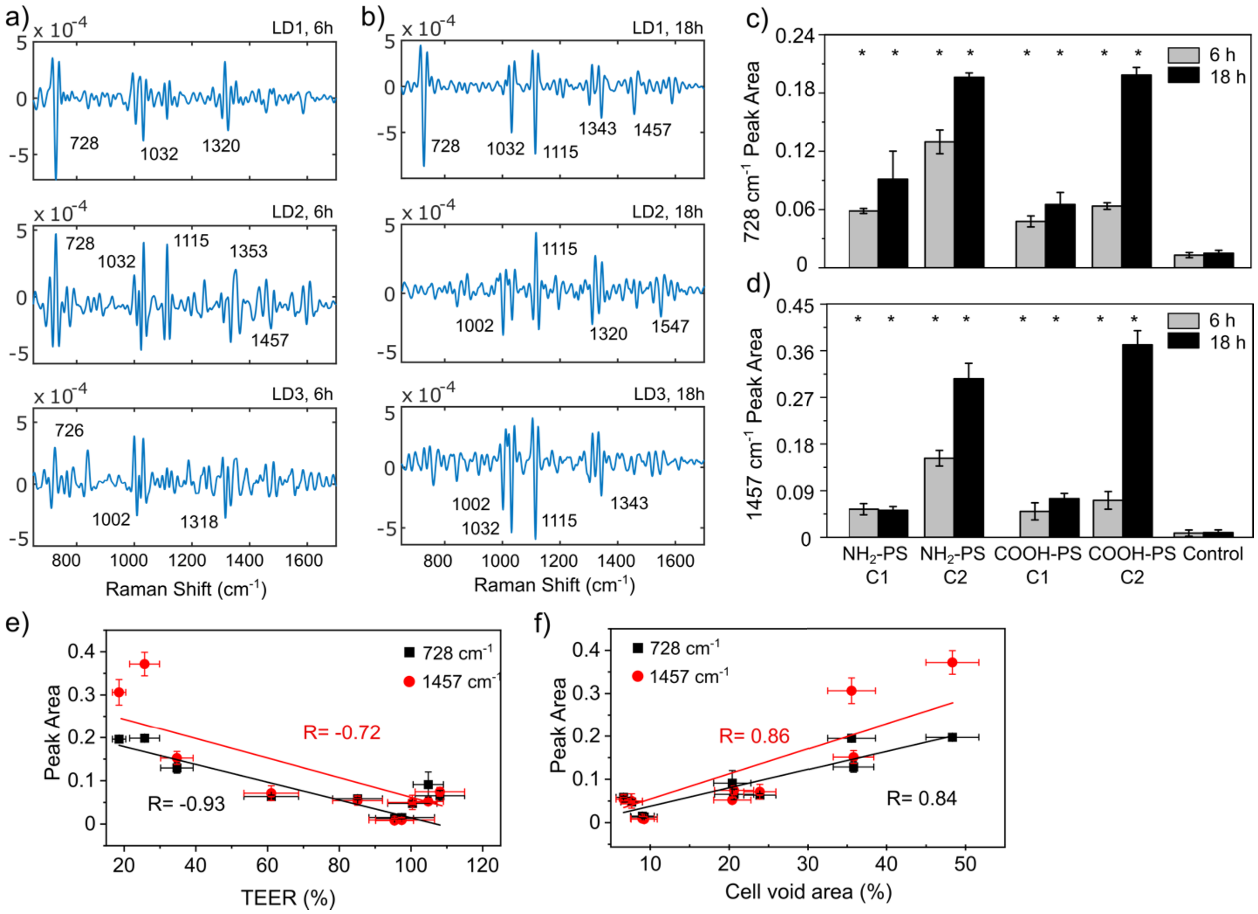

Figure 9: Loading spectra of the first three discriminants LD1-3 (top to bottom) for the data set recorded after a). 6 h and b). 18 h. c). Integrated area of the 728 cm^{-1}, d). 1457 cm^{-1} peak in the SERS spectra of Caco-2 monolayers treated with NH$_2$-PS (*C1*: 1x10^{12} NPs mL^{-1} and *C2*: 6x10^{12} NPs mL^{-1}), COOH-PS (*C1*: 6x10^{12} NPs mL^{-1} and *C2*: 1x10^{14} NPs mL^{-1}) for 6 h or 18 h, and Caco-2 cells without treatment as the control group. The peak areas were determined by Lorentzian fits. e). Peak area at 728 cm^{-1} and 1457 cm^{-1} as function of TEER value. Pearson correlation coefficient: -0.93 and -0.72. f). Peak area at 728 cm^{-1} and 1457 cm^{-1} as function of area of Caco-2 membrane void of cells in % at 18 h. Pearson correlation coefficient: 0.84 and 0.86. The data represent an average of n=25 independent experiments. * indicates a significant difference at the $p<0.05$ level.

of the no treatment control and PS NPs incubated cells, is characteristic of the ring-breathing modes in purines. Likewise, the peak at 1457 cm^{-1} lies in the range of C-N ring stretching modes of purines.

The purine vibrational features could indicate adenine, coenzyme A or hypoxanthine. We tested these three components under the identical experimental conditions and found coenzyme A ring-breathing peaks appeared at 734 cm^{-1} and 1430 cm^{-1}; hypoxanthine shows SERS peaks at 728 cm^{-1} and 1457 cm^{-1}; adenine has SERS peaks at 737 cm^{-1} and 1461 cm^{-1} (**Figure S4, S5**). So we determined that hypoxanthine provides the best fit.

While the modes at 1002 cm^{-1}, 1032 cm^{-1}, 1115 cm^{-1}, and 1320 cm^{-1} and 1340 cm^{-1}, indicative of phenylalanine, C-C or C-N stretching modes, and C-O and C-H stretching modes of lipids (**Table S2**) are common in the growth medium, the 728 cm^{-1} and 1457 cm^{-1} modes are rarely detected in the spectra of plain growth medium (**Figure S6).** The 728 cm^{-1} feature is, however, very prominent in the second derivative spectra of medium collected from cells treated with NH_2-PS (*C1* and *C2*) for 18 h, with NH_2-PS (*C2*) for 6 h, and with COOH-PS (*C2*) for 18 h (**Figure 6**). The integrated 728 cm^{-1} and 1457 cm^{-1} peak intensity, which correlate with the hypoxanthine concentration in the medium, are increased relative to the no treatment control for all PS-NP conditions (**Figure 9c, 9d**). The 728 cm^{-1} and 1457 cm^{-1} signal intensity are particularly high for NH_2-PS and COOH-PS with concentration *C2* at 18 h and to a somewhat lower degree for NH_2-PS (*C2*) at 6 h as well as for NH_2-PS (*C1*) at 18 h. The observation of increased 728 cm^{-1} and 1457 cm^{-1} peak intensities for conditions that result in increased Caco-2 membrane damage in **Figure 4b** and **4c** suggest a relationship between hypoxanthine concentration in the medium and Caco-2 cell damage. To formally test this hypothesis, we correlated the peak intensity at 728 cm^{-1} and 1457 cm^{-1} with TEER **(Figure 9e**) and the area in the Caco-2 cell monolayer void of cells (**Figure 9f**). The Pearson correlations coefficients of two peak intensity are R = -0.93 and -0.72, and R= 0.84 and 0.86, respectively. The strong (anti)correlation confirms that increased levels of hypoxanthine in the medium are associated with PS NPs induced cell stress and that they are particularly high under conditions that lead to cell death and increased permeability of the Caco-2 cell monolayer. Hypoxanthine acts as a marker for nanoplastics-induced damage to the Caco-2 intestinal membrane model. This interpretation is corroborated by previous studies that identified hypoxanthine as a marker for the dysregulation of epithelial cell membranes.[97] We determined a SERS detection limit of 10 nM for hypoxanthine in medium under our experimental conditions (**Figure S7**), which underlines the potential of SERS as sensitive diagnostics for intestinal stress metabolites with potential applications for monitoring intestinal membrane health both *in vitro* and *in vivo*.

3. Conclusion

We characterized PS NPs induced cellular stress in a monolayer of differentiated Caco2 cells and validated the applicability of SERS to identify NP-induced perturbation of the intestinal membrane model through spectral analysis of the extracellular medium. Multivariate analysis of the data achieved a spectral "fingerprinting" of the cellular response to the different PS NPs conditions: COOH-PS and NH_2-PS with concentrations *C1* and *C2* after 6 h and 18 h. At 18 h, it was possible not only to distinguish the PS NPs treated cells from the no treatment controls but also to distinguish different PS NPs conditions, which differed in surface chemistry (NH_2, COOH) and concentrations, from each other. Importantly, the SERS spectra of NH_2-PS and COOH-PS for both investigated concentrations *C1* and *C2* could already be reliably distinguished from the no treatment controls after 6 h, indicating a sensitive detection of PS NP-induced metabolomic changes even under conditions with little to no apparent intestinal membrane stress based on ROS, MTT, LDH or TEER measurements. The spectral differences become more pronounced under conditions for which a continuous non-reversible decrease in TEER indicates a loss in cell monolayer integrity. The spectra identified hypoxanthine as a metabolite in the extracellular medium that is correlated with NP-induced intestinal membrane damage.

The PS NPs concentrations required to induce membrane damage within a time window of 18 h investigated in this work are high, and uptake of these concentrations through food and water is unlikely. At the same time, the detection of spectral changes in the medium under conditions that do not show significant alterations in membrane permeability indicates the existence of more subtle NP-induced cellular changes that may give rise to detrimental effects on longer time scales than sampled in this study, especially under chronic exposure conditions. The ability to detect PS NP-induced changes in the metabolism of intestinal cells through SERS measurements of the extracellular medium provides a new tool for the quantitative characterization of NP-induced cellular stress that can be instrumental in assessing the risk associated with nanoplastics in future studies.

4. Methods

Cell Culture: The human colon carcinoma Caco-2 cell lines was purchased from the American Type Culture Collection (ATCC®, HTB-37™). The cells were grown in advanced Minimum Essential medium (MEM) supplemented with 10% fetal bovine serum, 50 units/mL penicillin, and grown in an incubator at 37 °C, 5% CO_2 and 95% relative humidity. The Caco-2 cells were seeded at a density of 1×10^5 cells per well on to transwell polyester membrane cell culture inserts (12 mm diameter, 0.4 μm pore size, Corning®). The growth medium was changed every 3 days. The cells were left to grow and differentiate for 21 days.

Characterization of PS-NPs: COOH-PS particles are commercially available from Polysciences (Fluoresbrite ® YG Carbxylate Microspheres, 0.05 μm, λ_{exc}/ λ_{em} =441 nm/ 486 nm). NH_2-PS particles are commercially available from Millipore Sigma (amine-modified polystyrene, fluorescent blue, 0.05 µm, Ex λ_{exc}/ λ_{em} =360 nm/ 420 nm). Both PS NPs were washed with Milli-Q water in centrifugal filter units (Amicon® Ultra-4, 10 kDa) for three times before experiments. Dynamic light scattering (DLS) measurement and zeta potential measurement were performed by Zetasizer Nano ZS90 (Malvern, Worestershire, UK). The hydrodynamic diameter of nanoparticles were measured at concentration of 1×10^{12} NPs mL^{-1} in Milli-Q water. Zeta potential of nanoparticles were measured at concertation of 1×10^{12} NPs mL^{-1} in 10 mM NaCl (pH 7.0). The reported results represent the mean of 10 independent experiments.

Colloidal Au NP Synthesis: Colloidal gold seeds were prepared by heating 20 mL of $HAuCl_4 \cdot 3H_2O$ (0.26 mM, Sigma-Aldrich, wt 393.83 g), and adding 800 µL of sodium citrate dihydrate (34.00 mM, Sigma-Aldrich, wt 294.10 g) immediately after boiling. The gold seeds were then grown to an average size of 40 nm by adding dropwise 50 ml of $HAuCl_4.3H_2O$ solution (1.00 mM), and 80 mL of a mixture of sodium citrate dihydrate (0.85 mM) and L-Ascorbic acid (2.84 mM, Sigma-Aldrich, wt 176.12 g). The 80 nm gold nanoparticles were obtained by adding 80 ml of mixture prepared above. The gold solution was then boiled for 30 min and neutralized to pH 7.0 with a 10 mM aqueous solution of NaOH (Sigma-Aldrich, wt 40.00 g). Before use, the colloidal gold solution was washed by centrifugation (720g, 10 min) and resuspension in Milli-Q water.

Preparation of SERS Substrate: Aqueous solutions of 80 nm AuNPs ($1x10^{12}$ NPs ml^{-1} , 5 ml) were prepared as described above. 5 mL of hexane was added to form the water-hexane interface. Then ethanol was added dropwisely. The hexane layer on the top was removed, and the Au NP film formed on the water surface was carefully transferred to a glass coverslip. The prepared substrate was placed in the hood overnight to evaporate residual solvent.

Dark-Field Scattering Characterization of SERS Substrate: Scattering images of Au film were recorded using an upright microscope (Olympus BX51 WI). The scattering behavior the sample was characterized with unpolarized white light fitted with an air dark-field condenser in transmission mode. Light scattering from the Au NP film was collected using a 60x oil immersion objective (NA =0.65). The microscope featured a 303 mm focal length imaging spectrometer (Andor Shamrock) and a back-illuminated CCD detector (DU401-BR-DD). The recorded spectra were corrected by subtracting the background signal originating from an adjacent area on the glass slide without Au NP film, and normalized by division through the excitation profile of the white light illumination source.

Quantification of PS uptake: Specified concentration of NH_2-PS and COOH-PS in growth medium was placed into the apical chamber. Cells were incubated with particles at 37 °C and 5% CO_2 for 6 h, 18 h. Cells were washed twice with Dulbeccos Phosphate-Buffered Saline (DPBS) and followed by detachment with cell dissociation buffer. The cell suspension were collected and move into a microplate, where the fluorescence intensity was measured at an excitation wavelength of 546 nm and emission wavelength of 561 nm for NH_2-PS (488 nm and 520 nm for COOH-PS) using a microplate reader. Cells were stained with 0.2% trypan blue, and the cell number was counted with a cell counter. The number of polystyrene particles being uptaken was determined with a calibration curve of fluorescence intensity as function of NP concentration.

Mapping Intracellular Particle Distribution through Confocal Microscopy: Cells were fixed with 4% (w/v) Pierce^{TM} Formaldehye (ThermoFisher) for 15 min. Subsequently, the cells were incubated with ZO-1 Monoclonal Antibody, Alexa Fluor 647 (10 ug ml^{-1}, ThermoFisher), Hoechst 33342 (400 ng ml^{-1}, Invitrogen, USA) at room temperature for 1 hour. The cells were washed three times with DPBS after each step of the fixation and labeling procedure to remove excess reagents.

Samples were imaged with scanning confocal microscope (Olympus FV 1000) at 405,488 and 647 nm.

Optical Inspection of Live and Dead Cells in Caco-2 Monolayers: After NP treatment, Caco-2 cells were stained with Calcein-AM (2µM) and EthD-1 (4 µM) for 45 min at room temperature. The cells were imaged in an inverted microscope (Olympus IX71) through a 10x objective, and signal captured on an electron multiplying CCD (EMCCD, Andor Ixon$^+$). The fluorescent signal of live cell was measured with excitation/ emission wavelengths of 473 nm and 510 nm. The fluorescent signal of dead cell was measured at an excitation and an emission wavelength of 580 nm and 620 nm. The exposure time for each monochromatic image was 0.5 s, and the cycle time for a full set of ten images was 5 s.

Cell Viability Measurement: Cell viability was measured using the Vybrant™ MTT Cell Proliferation Assay kit (Invitrogen) following the manual instructions. After PS NPs treatment, cell were incubated with MTT working solution (1mM) at 37 °C for 2 hours, and followed with 50 µl of DMSO as solubilization solution. The absorbance was measured at 540 nm. The percentage of cell viability change was compared with cell viability from the control group.

ROS Level Measurement: Intracellular ROS level was detected using 10 µM of 2’, 7’ – dichlorofluorescin diacetate (DCFH-DA; Sigma Aldrich, USA) at 37 °C for 45 min. The DCF intensity was measured at an excitation and an emission wavelength of 488 nm and 525 nm. H_2O_2 (200 µM) treated Caco-2 cells were used as positive control. The percentage of ROS level change was compared with ROS level from the no treatment control group.

LDH Measurements: LDH leakage was measured from Caco-2 cells using a CyQUANT™ LDH Cytotoxicity Assay kit (Invitrogen, C20300) following the manual instructions. After PS NP treatment, 50 µl of cell growth medium were collected from the apical compartment and 50 µl of LDH reaction mixture was added. The wells were incubated for 30 min at room temperature, followed by 50 µl stop solution. The absorbance was measured at 490 nm. The percentage of LDH activity change was determined relative to the LDH release from the no treatment control group.

TEER measurements: The trans-epithelial electrical resistance (TEER) of the cell monolayers were measured using a Millicell-ERS Voltammeter (Millipore Sigma). To eliminate the influence of temperature, measures were performed within 2 min after taking the transwell cell culture plate out of the incubator. Within this time, samples did not show any reading drift. Prior to the measurements, electrodes were equilibrated and sterilized according to the manufacturer's recommendations. The TEER of the cell monolayer was measured every three days after seeding to assess cell confluency and tight junction functionality. Only cells with an average TEER value 700 Ohms are qualified for further experiments. During particle treatment, TEER were recorded every hour for 24 h. Three measurements were taken per cell sample. The normalized TEER was calculated by dividing the measurements with the TEER obtained before particle treatment (t=0).

SERS Measurements: 20 µl of cell medium was pipetted onto the SERS substrate. Then a glass coverslip was placed on the top to prevent evaporation of cell medium during the SERS measurement. The spectra were obtained with a Renishaw Raman microscope (model RM-2000) using a 50 x objective. The sample were excited by a diode laser with 785 nm wavelength and an excitation power of 0.7 mW. All spectra were obtained with a 10 s integration time, and 10 spectra were accumulated

Data Processing and Analysis: All data were imported into MatLab (The Mathworks Inc., Natick, MA) and an initial data processing and analysis was performed with the PLS toolbox (Eigenvector Research, Wenatchee, WA). The spectra was baseline corrected using a Whittaker filter (λ=200) and area-normalized (n = 1). The second derivatives spectra was calculated after a Savitzky-Golay smoothing (filter width ω= 15, polynomial order σ= 2) using the PLS toolbox. The obtained second derivative spectra were converted into a barcode spectra using a home-written program. Raman shifts with a negative second derivative whose absolute value was at least 2.5 standard deviations higher than the noise were assigned a value of 1. All other Raman shifts were assigned a value of 0. The bar code of all the spectra of one condition were added and normalized to generate histograms of the second derivative spectra. t-SNE of the second derivative spectra (no barcoding) was performed with the Matlab t-SNE function. PCA of the second derivative spectra was performed using the Matlab PCA function. The first 20 PCs were used as input for an LDA analysis implemented as described by Chen and Hsu in Matlab. [96] Spectral peak areas were obtained from baseline- and area-corrected spectra through fitting of Lorentzian peak function $y = y_0 + \frac{2A}{\pi}\frac{\omega}{4(x-x_c)^2+\omega^2}$ (A= area, ω= width, x_c= spectral peak).

Supporting Information

Supporting Information is available from the Wiley Online Library or from the author.

Acknowledgement

B.M.R. acknowledges support from the National Science Foundations through grants CBET-1822246 and CBET-2032376.

References

[1] PlasticsEurope, Plastics-the Facts 2020, https://www.plasticseurope.org/en/resources/market-data, accessed: November, **2020**.

[2] Shah, A. A.; Hasan, F.; Hameed, A.; Ahmed, S. Biological Degradation of Plastics: A Comprehensive Review. *Biotechnol. Adv.* **2008**, *26*, 246-265.

[3] Frias, J. P. G. L.; Nash, R. Microplastics: Finding A Consensus on The Definition. *Mar. Pollut. Bull.* **2019**, *138*, 145-147.

[4] Thompson, R. C.; Olsen, Y.; Mitchell, R. P.; Davis, A.; Rowland, S. J.; John, A. W.; McGonigle, D.; Russel, A. E. Lost At Sea: Where Is All The Plastic? *Science* **2004**, *304*, 838.

[5] Desai, M. P.; Labhasetwar, V.; Amidon, G. L.; Levy, R. J. Gastrointestinal Uptake of Biodegradable Microparticles: Effect of Particle Size. *Pharm. Res.* **1996**, *13*, 1838-1845.

[6] Frohlich, E.; Roblegg, E. Models for Oral Uptake of Nanoparticles in Consumer Products. *Toxicology* **2012**, *291*, 10-17.

[7] Hillyer, J. F.; Albrecht, R. M. Gastrointestinal Persorption and Tissue Distribution of Differently Sized Colloidal Gold Nanoparticles. *J. Pharm. Sci.* **2001**, *90*, 1927-1936.

[8] Verma, A.; Stellacci, F. Effect of Surface Properties on Nanoparticle-Cell Interactions. *Small* **2010**, *6*, 12-21.

[9] Septiadi, D.; Crippa, F.; Moore, T. L.; Rothen-Rutishauser, B.; Petri-Fink, A. Nanoparticle-Cell Interaction: A Cell Mechanics Perspective. *Adv. Mater.* **2018**, *30*, 1704463.

[10] Naasz, S.; Altenburger, R.; Kuhnel, D. Environmental Mixtures Of Nanomaterials And Chemicals: The Trojan-Horse Phenomenon and Its Relevance for Ecotoxicity. *Sci. Total. Environ.* **2018**, *635*, 1170-1181.

[11] Borm, P. J. A. Particle Toxicology: From Coal Mining to Nanotechnology. *Inhal. Toxicol.* **2002**, *14*, 311-324.

[12] Balbus, J. M.; Maynard, A. D.; Colvin, V. L.; Castranova, V.; Daston, G. P.; Denison, R. A.; Dreher, K. L.; Goering, P. L.; Goldberg, A. M.; Kulinowski, K. M.; Monteiro-Riviere, N. A.; Oberdorster, G.; Omenn, G. S.; Pinkerton, K. E.; Ramos, K. S.; Rest, K. M.; Sass, J. B.; Silbergeld, E. K.; Wong, B. A. Meeting Report: Hazard Assessment for Nanoparticles--Report from An Interdisciplinary Workshop. *Environ. Health Perspects.* **2007**, *115*, 1654-1659.

[13] Lewinski, N.; Colvin, V.; Drezek, R. Cytotoxicity of Nanoparticles. *Small* **2008**, *4*, 26-49.

[14] Park, M. V. D. Z.; Neigh, A. M.; Vermeulen, J. P.; de la Fonteyne, L. J. J.; Verharen, H. W.; Briede, J. J.; van Loveren, H.; de Jong, W. H. The Effect of Particle Size on The Cytotoxicity, Inflammation, Developmental Toxicity and Genotoxicity of Silver Nanoparticles. *Biomaterials* **2011**, *32*, 9810-9817.

[15] Manke, A.; Wang, L.; Rojanasakul, Y. Mechanisms of Nanoparticle-Induced Oxidative Stress and Toxicity. *Biomed Res. Int.* **2013**, *2013*, 942916.

[16] Bouwmeester, H.; van der Zande, M.; Jepson, M. A. Effects of Food-Borne Nanomaterials on Gastrointestinal Tissues And Microbiota. *WIREs Nanomed Nanobiotechnol.* **2018**, 10:e1481.

[17] Lambert, S.; Wagner, M. Formation of Microscopic Particles during The Degradation of Different Polymers. *Chemosphere* **2016**, *161*, 510-517.

[18] Ward, J. E.; Kach, D. J. Marine Aggregates Facilitate Ingestion of Nanoparticles by Suspension-Feeding Bivalves. *Mar. Environ. Res.* **2009**, *68*, 137-142.

[19] Bhattacharya, P.; Lin, S.; Turner, J. P.; Ke, P. C. Physical Adsorption of Charged Plastic Nanoparticles Affects Algal Photosynthesis. *J. Phys. Chem. C.* **2010**, *114*, 16556-16561.

[20] Besseling, E.; Wang, B.; Lurling, M.; Koelmans, A. A. Nanoplastic Affects Growth of *S. Obliquus* And Reproduction of *D. Magna*. *Environ. Sci. Technol.* **2014**, *48*, 12336-12343.

[21] Alvarez-Roman, R.; Naik, A.; Kalia, Y. N.; Guy, R. H.; Fessi, H. Skin Penetration And Distribution of Polymeric Nanoparticles. *J. Control. Release* **2004**, *99*, 53-62. 24

[22] Grafmueller, S.; Manser, P.; Diener, L.; Diener, P. A.; Maeder-Althaus, X.; Maurizi, L.; Jochum, W.; Krug, H. F.; Buerki-Thurnherr, T.; von Mandach, U.; Wick, P. Bidirectional Transfer Study of Polystyrene Nanoparticles

across The Placental Barrier in An *ex Vivo* Human Placental Perfusion Model. *Environ. Health Perspect.* **2015**, *123*, 1280-1286.

[23] Yang, C.-S.; Chang, C.-H.; Tsai, P.-J.; Chen, W.-Y.; Tseng, F.-G.; Lo, L.-W. Nanoparticle-Based in Vivo Investigation on Blood-Brain Barrier Permeability Following Ischemia And Reperfusion. *Anal. Chem.* **2004**, *76*, 4465-4471.

[24] Elamin, E.; Jonkers, D.; Juuti-Uusitalo, K.; van Ijzendoorn, S.; Troost, F.; Duimel, H.; Broers, J.; Verheyen, F.; Dekker, J.; Masclee, A. Effects of Ethanol And Acetaldehyde on Tight Junction Integrity: *in Vitro* Study in A Three Dimensional Intestinal Epithelial Cell Culture Model. *PLos One* **2012**, *7*, e35008.

[25] Elamin, E.; Masclee, A.; Juuti-Uusitalo, K.; van Ijzendoorn, S.; Troost, F.; Pieters, H.-J.; Dekker, J.; Jonkers, D. Fatty Acid Ethyl Esters Induce Intestinal Epithelial Barrier Dysfunction via A Reactive Oxygen Species-Dependent Mechanism in A Three-Dimensional Cell Culture Model. *PLoS One* **2013**, *8*, e58561.

[26] Garcia-Castillo, M. D.; Chinnapen, D. J.-F.; Lencer, W. I. Membrane Transport across Polarized Epithelia. *Cold Spring Harb. Perspect. Biol.* **2017**, *9*, a027912. 29

[27] Fowler, R.; Vllasaliu, D.; Trillo, F. F.; Garnett, M. C.; Alexander, C.; Horsley, H.; Smith, B.; Whitcombe, I.; Eaton, M.; Stolnik, S. Nanoparticle Transport in Epithelial Cells: Pathway Switching through Bioconjugation. *Small* **2013**, *9*, 3282-3294.

[28] Pridgen, E. M.; Alexis, F.; Kuo, T. T.; Levvy-Nissenbaum, E.; Karnik, R.; Blumberg, R. S.; Langer, R.; Farokhzad, O. C. Transepithelial Transport of Fc-Targeted Nanoparticles by The Neonatal Fc Receptor for Oral Delivery. *Sci. Transl. Med.* **2013**, *5*, 213ra167.

[29] Yun, Y.; Cho, Y. W.; Park, K. Nanoparticles for Oral Delivery: Targeted Nanoparticles with Peptidic Ligands for Oral Protein Delivery. *Adv. Drug. Deliv. Rev.* **2013**, *65*, 822-832.

[30] Thubagere, A.; Reinhard, B. M. Nanoparticle-Induced Apoptosis Propagates through Hydrogen-Peroxide-Mediated Bystander Killing: Insights from A Human Intestinal Epithelium *in Vitro* Model. *ACS Nano* **2010**, *4*, 3611-3622.

[31] Veiseh, O.; Tang, B. C.; Whitehead, K. A.; Anderson, D. G.; Langer, R. Managing Diabetes with Nanomedicine: Challenges And Opportunities. *Nat. Rev. Drug Discov.* **2015**, *14*, 45-57.

[32] des Rieux, A.; Fievvez, V.; Theate, I.; Mast, J.; Preat, V.; Schneider, Y.-J. An Improved in Vitro Model of Human Intestinal Follicle-Associated Epithelium to Study Nanoparticle Transport by M Cells. *Eur. J. Pharm. Sci.* **2007**, *30*, 380-391.

[33] Yacobi, N. R.; Demaio, L.; Xie, J.; Hamm-Alvarez, S. F.; Borok, Z.; Kim, K.-J.; Crandall, E. D. Polystyrene Nanoparticle Trafficking across Alveolar Epithelium. *Nanomedicine* **2008**, *4*, 139-145.

[34] Bannunah, A. M.; Vllasaliu, D.; Lord, J.; Stolnik, S. Mechanisms of Nanoparticle Internalization and Transport across An Intestinal Epithelial

Cell Model: Effect of Size And Surface Charge. *Mol. Pharmaceutics* **2014**, *11*, 4363-4373.

[35] Behrens, I.; Pena, A. I. V.; Alonso, M. J.; Kissel, T. Comparative Uptake Studies of Bioadhesive and Non-Bioadhesive Nanoparticles in Human Intestinal Cell Lines and Rats: The Effect of Mucus on Particle Adsorption And Transport. *Pharm. Res.* **2002**, *19*, 1185-1193.

[36] Mahler, G. J.; Esch, M. B.; Tako, E.; Southard, T. L.; Archer, S. D.; Glahn, R. P.; Shuler, M. L. Oral Exposure to Polystyrene Nanoparticles Affects Iron Absorption. *Nat Nanotechnol.* **2012**, *7*, 264-271.

[37] Cortes, C.; Domenech, J.; Salazar, M.; Pastor, S.; Marcos, R.; Hernandez, A. Nanoplastics as A Potential Environmental Health Factor: Effects of Polystyrene Nanoparticles on Human Intestinal Epithelia Caco-2 Cells. *Environ. Sci.Nano* **2020**, *7*, 272.

[38] Paget, V.; Dekali, S.; Kortulewski, T.; Grall, R.; Gamez, C.; Blazy, K.; Aguerre-Chariol, O.; Chevillard, S.; Braun, A.; Rat, P.; Lacroix, G. Specific Uptake And Genotoxicity Induced by Polystyrene Nanobeads with Distinct Surface Chemistry on Human Lung Epithelial Cells and Macrophages. *PLoS One* **2015**, *10*, e0123297.

[39] Pinto, M.; Robine-Leon, S.; Appay, M. D. Enterocyte-Like Differentiation And Polarization of The Human-Colon Carcinoma Cell-Line Caco-2 in Culture. *Biol. Cell* **1983**, *47*, 323-330.

[40] Artursson, P. Epithelial Transport of Drugs in Cell-Culture .I: a Model for Studying The Passive Diffusion of Drugs over Intestinal Absorptive (Caco-2) Cells. *J. Pharm. Sci.* **1990**, *79*, 476-482.

[41] Hilgers, A. R.; Conradi, R.; Burton, P.S. Caco-2 Cell Monolayers as A Model for Drug Transport across The Intestinal Mucosa. *Pharm. Res.* **1990**, *7*, 902-910.

[42] Artursson, P.; Borchardt, R. T. Intestinal Drug Absorption And Metabolism in Cell Cultures: Caco-2 and Beyond. *Pharm. Res.* **1997**, *14*, 1655-1658.

[43] Konsoula, R.; Barile, F. A. Correlation of *in Vitro* Cytotoxicity with Paracellular Permeability in Caco-2 Cells. *Toxicol. In Vitro* **2005**, *19*, 675-684.

[44] Okada, T.; Narai, A.; Matsunga, S.; Fusetani, N.; Shimizu, M. Assessment of The Marine Toxins by Monitoring The Integrity of Human Intestinal Caco-2 Cell Monolayers. *Toxicol. In Vitro* **2000**, *14*, 219-226.

[45] Sha, X.; Yan, G.; Wu, Y.; Li, J.; Fang, X. Effect of Self-Microemulsifying Drug Delivery Systems Containing Labrasol on Tight Junctions in Caco-2 Cells. *Eur. J. Pharm. Sci.* **2005**, *24*, 477-486.

[46] Domenech, J.; Hernandez, A.; Rubio, L.; Marcos, R.; Cortes, C. Interactions of Polystyrene Nanoplastics with *in Vitro* Models of The Human Intesintal Barrier. *Arch. Toxicol.* **2020**, *94*, 2997-3012.

[47] Liu, S.; Wu, X.; Gu, W.; Yu, J.; Wu, B. Influence of The Digestive Process on Intestinal Toxicity of Polysytrene Microplastics as Determined by *in Vitro* Caco-2 Models. *Chemosphere* **2020**, *356*, 127204.

[48] Win, K. Y.; Feng, S.-S. Effects of Particle Size And Surface Coating on Cellular Uptake of Polymeric Nanoparticles for Oral Delivery of Anticancer Drugs. *Biomaterials* **2005**, *26*, 2713-2722.

[49] Hu, C.-S.; Chiang, C.-H.; Hong, P.-D.; Yeh, M.-K. Influence of Charge on FITC-BSA-Loaded Chondroitin Sulfate-Chitosan Nanoparticles upon Cell Uptake in Human Caco-2 Cell Monolayers. *Int. J. Nanomedicine* **2012**, *7*, 4861-4872.

[50] Loh, J. W.; Saunders, M.; Lim, L.-Y. Cytotoxicity of Monodispersed Chitosan Nanoparticles against Caco-2 Cells. *Toxicol. Appl. Pharmacol.* **2012**, *262*, 273-282.

[51] Jin, C.; Liu, Y.; Sun, L.; Chen, T.; Zhang, Y.; Zhao, A.; Wang, X.; Cristau, M.; Wang, K.; Jia, W. Metabolic Profiling Reveals Disorder of Carbohydrate Metabolism in Mouse Fibroblast Cells Induced by Titanium Dioxide Nanoparticles. *J. Appl. Toxicol.* **2013**, *33*, 1442-1450.

[52] Bo, Y.; Jin, C.; Liu, Y.; Yu, W.; Kang, H. Metabolomic Analysis on The Toxicological Effects of TiO_2 Nanoparticles in Mouse Fibroblast Cells: from The Perspective of Perturbations in Amino Acid Metabolism. *Toxicol. Mech. Methods* **2014**, *24*, 461-469.

[53] Zhang, J. L.; Zhou, Z. P.; Pei, Y.; Xiang, Q. Q.; Chang, X. X.; Ling, J.; Shea, D.; Chen, L. Q. Metabolic Profiling of Silver Nanoparticle Toxicity in Microcystis Aeruginosa. *Environ. Sci. Nano* **2018**, *5*, 2519.

[54] Shim, W.; Paik, M. J.; Nguyen, D.-T.; Lee, J.-K.; Lee, Y.; Kim, J.-H.; Shin, E.-H.; Kang, J. S.; Jung, H.-S.; Choi, S.; Park, S.; Shim, J. S., Lee, G.

Analysis of Changes in Gene Expression And Metabolic Profiles Inudced by Silica-Coated Magnetic Nanoparticles. *ACS Nano* **2012,** *6*, 7665-7680.

[55] Plou, J.; Garcia, I.; Charconnet, M.; Astobiza, I.; Garcia-Astrain, C.; Matricardi, C.; Mihi, A.; Carracedo, A.; Liz-Marzan, L. M. Multiplex SERS Detection of Metabolic Alterations in Tumor Extracellular Media. *Adv. Funct. Mater.* **2020**, *30*, 1910335.

[56] Lussier, F.; Missirlis, D.; Spatz, J. P.; Masson, J.-F. Machine-Learning-Driven Surface-Enhanced Raman Scattering Optophysiology Reveals Multiplexed Metabolite Gradients Near Cells. *ACS Nano* **2019**, *13*, 1403-1411.

[57] Ali, M. R. K.; Wu, Y.; Han, T.; Zang, X.; Xiao, H.; Tang, Y.; Wu, R.; Fernandez, F. M.; EI-Sayed, M. A. Simultaneous Time-Dependent Surface-Enhanced Raman Spectroscopy, Metabolomics, And Proteomis Reveal Cancer Cell Death Mechanisms Associated with Gold Nanorod Photothermal Therapy. *J. Am. Chem. Soc.* **2016**, *38*, 15434-15442.

[58] Premasiri, W. R.; Lee, J. C.; Sauer-Budge, A.; Theberge, R.; Costello, C. E.; Ziegler, L. D. The Biochemical Origins of The Surface-Enhanced Raman Spectra Of Bacteria: A Metabolomics Profiling by SERS. *Anal. Bioanal. Chem.* **2016**, *408*, 4631-4647.

[59] Shalabaeva, V.; Lovato, L.; La Rocca, R.; Messina, G. C.; Dipalo, M.; Miele, E.; Perrone, M.; Gentile, F.; De Angelis, F. Time Resolved And Label Free Monitoring of Extracellular Metabolites by Surface Enhanced Raman Spectroscopy. *PLoS One* **2017**, *12*, e0175581.

[60] Sherman, L.M.; Petrov, A. P.; Karger, L. F. P.; Tetrick, M. G.; Dovichi, N. J.; Camden, J. P. A Surface-Enhanced Raman Spectroscopy Database of 63 Metabolites. *Talanta* **2020**, *210*, 120645.

[61] Li, L.; Xiao, R.; Wang, Q.; Rong, Z.; Zhang, X.; Zhou, P.; Fu, H.; Wang, S.; Wang, Z. SERS Detection of Radiation Injury Biomarkers in Mouse Serum. *RSC Adv.* **2018**, *8*, 5119.

[62] Wang, Z.-y.; Li, W.; Gong, Z.; Sun, P.-r.; Zhou, T.; Cao, X.-w. Detection of IL-8 in Human Serum Using Surface-Enhanced Raman Scattering Coupled with Highly-Branched Gold Nanoparticles And Gold Nanocages. *New J. Chem.* **2019**, *43*, 1733.

[63] Lee, C. H.; Hankus, M. E.; Tian, L.; Pellegrino, P. M.; Singamaneni, S. Highly Sensitive Surface Enhanced Raman Scattering Substrates Based on Filter Paper Loaded with Plasmonic Nanostrucutres. *Anal. Chem*. **2011**, *83*, 8953-8958.

[64] Haynes, C. L.; McFarland, A. D.; Van Duyne, R. P. Surface-Enhanced Raman Spectroscopy. *Anal. Chem.* **2005**, *77*, 338a-346a.

[65] Yan, B.; Thubagere, A.; Premasiri, R. W.; Ziegler, L. D.; Dal Negro, L.; Reinhard, B. M. Engineered SERS Substrates with Multiscale Signal Enhancement: Nanoparticle Cluster Arrays. *ACS Nano* **2009**, *3*, 1190 - 1202.

[66] Yang, L.; Yan, B.; Premasiri, R. W.; Ziegler, L. D.; Dal Negro, L.; Reinhard, B. M. Engineering Nanoparticle Cluster Arrays for Bacterial Biosensing: The Role of the Building Block in Multiscale SERS Substrates. *Adv. Funct. Mater.* **2010**, *20*, 2619-2628.

[67] Yan, B.; Boriskina, S. V.; Reinhard, B. M. Design and Implementation of Noble Metal Nanoparticle Cluster Arrays for Plasmon Enhanced Biosensing. *J. Phys. Chem.C* **2011**, *115*, 24437-24453.

[68] Cedervall, T.; Lynch, I.; Lindman, S.; Berggard, T.; Thulin, E.; Nilsson, H.; Dawson, K. A.; Linse, S. Understanding The Nanoparticle-Protein Corona Using Methods to Quantify Exchange Rates And Afinities of Proteins to Nanoparticles. *PNAS* **2007**, *104*, 2050-2055.

[69] Lundqvist, M.; Stigler, J.; Elia, G.; Lynch, I.; Cedervall, T.; Dawson, K. A. Nanoparticle Size And Surface Properties Determine The Protein Corona with Possible Implications for Biological Impacts. *PNAS* **2008**, *105*, 14265-14270.

[70] Xu, F.; Reiser, M.; Yu, X.; Gummuluru, S.; Wetzler, L.; Reinhard, B. M. Lipid Mediated Targeting with Membrane-Wrapped Nanoparticles in The Presence of Corona Formation. *ACS Nano* **2016**, *10*, 1189-1200.

[71] He, B.; Lin, P.; Jia, Z.; Du, W.; Qu, W.; Yuan, L.; Dai, W.; Zhang, H.; Wang, X.; Wang, J.; Zhang, X.; Zhang, Q. The Transport Mechanisms of Polymer Nanoparticles in Caco-2 Epithelial Cells. *Biomaterials* **2013**, *34*, 6082-6098.

[72] Song, Q.; Yao, L.; Huang, M.; Hu, Q.; Lu, Q.; Wu, B.; Qi, H.; Rong, Z.; Jiang, X.; Gao, X.; Chen, J.; Chen, H. Mechanisms of Transcellular Transport of Wheat Germ Agglutinin-Functionalized Polymeric Nanoparticles in Caco-2 Cells. *Biomaterials* **2012**, *33*, 6769-6782.

[73] Sheng, J.; Han, L.; Qin, J.; Ru, G.; Li, R.; Wu, L.; Cui, D.; Yang, P.; He, Y.; Wang, J. *N*-Trimethyl Chitosan Chloride-Coated PLGA Nanoparticles

Overcoming Multiple Barriers to Oral Insulin Absorption. *ACS Appl. Mater. Interfaces* **2015**, *7*, 15430-15441.

[74] van der Zande, M.; Undas, A. K.; Kramer, E.; Monopoli, M. P.; Peters, R. J.; Garry, D.; Fernandes, E. C. A.; Hendriksen, P. J.; Marvin, H. J. P.; Peijnenburg, A. A.; Bouwmeester, H. Different Responses of Caco-2 And MCF-7 Cells to Silver Nanoparticles Are Based on Highly Similar Mechanisms of Action. *Nanotoxicology* **2016**, *10*, 1431-1441.

[75] Ye, D.; Dawson, K.,A.; Lynch, L. A. TEM protocol for quality assurance of in vitro cellular barrier models and its application to the assessment of nanoparticle transport mechanisms across barriers. *Analyst* **2015**, 140, 83.

[76] Kararli, T.T. Comparison of the gastrointestinal anatomy, physiology, and biochemistry of humans and commonly used laboratory animals. *Biopharm. Drug. Dispos.* **1995**, 16, 351-380.

[77] DeSesso, J.M.; Jacobson, C.F. Anatomical and physiological parameters affecting gastrointestinal absorption in human and rats. *Food. Chem. Toxicol.* **2001**, 39, 209-228.

[78] Abstiens, K.; Figueroa, S. M.; Gregoritza, M.; Goepferich, A. M. Interaction of Functionalized Nanoparticles with Serum Proteins And Its Impact on Colloidal Stability And Cargo Leaching. *Soft Matter* **2019**, *15*, 709-720.

[79] Lesniak, A.; Salvati, A.; Santos-Martinez, M. J.; Radomski, M. W.; Dawson, K. A.; Aberg, C. Nanoparticle Adhesion to The Cell Membrane And Its

Effect on Nanoparticle Uptake Efficiency. *J. Am. Chem. Soc.* **2013**, *135*, 1438-1444.

[80] Tenzer, S.; Docter, D.; Kuharev, J.; Musyanovych, A.; Fetz, V.; Hecht, R.; Schlenk, F.; Fischer, D.; Kiouptsi, K.; Reinhardt, C.; Landfester, L.; Schild, H., Maskos, M.; Knauer, S. K.; Stauber, R. H. Rapid Formation of Plasma Protein Corona Critically Affects Nanoparticle Pathophysiology. *Nat. Nanotechnol.* **2013**, 8, 772-781.

[81] Kim, H. R.; Andrieux, K.; Gil, S.; Taverna, M.; Chacun, H.; Desmaele, D.; Taran, F.; Georgin, D.; Couvreur, P. Translocation of Poly(ethylene glycol-*co*-hexadecyl)cyanoacrylate Nanoparticles into Rat Brain Endothelial Cells: Role of Apolipoproteins in Receptor-Mediated Endocytosis. *Biomacromolecules* **2007**, *8*, 793-799.

[82] Gerloff, K.; Albrecht, C.; Boots, A. W.; Foster, I.; Schins, R. P. F. Cytotoxicity And Oxidative Damage by Nanoparticles in Human Intestinal Caco-2 Cells. *Nanotoxicology* **2009**, *3*, 355-364.

[83] Gerloff, K.; Pereira, D. I. A.; Faria, N.; Boots, A. W.; Kolling, J.; Forster, I.; Albrecht, C.; Powell, J. J.; Schins, R. P. F. Influence of Simulated Gastrointestinal Conditions on Particle-Induced Cytotoxicity And Interleukin-8 Regulation in Differentiated And Undifferentiated Caco-2 Cells. *Nanotoxicology* **2013**, *7*, 353-366.

[84] Kang, T.; Guan, R.; Chen, X.; Song, Y.; Jiang, H.; Zhao, J. *In Vitro* Toxicity of Different-Sized ZnO Nanoparticles in Caco-2 Cells. *Nanoscale Res. Lett.* **2013**, *8*, 496.

[85] Shalaev, V. M.; Botet, R.; Tsai, D. P.; Kovacs, J.; Moskovits, M. Fractals: Localization of Dipole Excitations and Giant Optical Polarizabilities. *Physica A* **1994**, *207*, 197-207.

[86] Yan, B.; Boriskina, S. V.; Reinhard, B. M. Optimizing Gold Nanoparticle Cluster Configurations ($n \leq 7$) for Array Applications. *J. Phys. Chem. C* **2011**, *115*, 4578-4583.

[87] Sun, F.; Ella-Menye, J.-R.; Galvan, D. D.; Bai, T.; Hung, H.-C.; Chou, Y.-N.; Zhang, P.; Jiang, S.; Yu, Q. Stealth Surface Modification of Surface-Enhanced Raman Scattering Substrates for Sensitive And Accurate Detection in Protein Solutions. *ACS Nano* **2015**, *9*, 2668-2676.

[88] Sun, F.; Hung, H.-C.; Sinclair, A.; Zhang, P.; Bai, T.; Galvan, D. D.; Jain, P.; Li, B.; Jiang, S.; Yu, Q. Hierarchical Zwitterionic Modification of A SERS Substrate Enable Real-Time Drug Moniotring in Blood Plasma. *Nat. Commun* **2016**, 7, 13437.

[89] Yonzon, C. R.; Haynes, C. L.; Zhang, X.; Walsh, J. T.; Van Duyne, R. P. A Glucose Biosensor Based on Surface-Enhanced Raman Scattering: Improved Partition Layer, Temporal Stability, Reversibility , And Resistance to Serum Protein Interference. *Anal. Chem*. **2004**, *76*,78-85.

[90] Miranda, O. R.; Creran, B.; Rotello, V. M. Array-Based Sensing with Nanoparitles: “Chemcial Noses” for Sensing Biomolecules And Cell Surfaces. *Curr Opin Chem Biol* **2010**, *14*, 728-736.

[91] Kim, N.; Thomas, M. R.; Bergholt, M. S.; Pence, I. J.; Seong, H.; Charchar, P.; Todorova, N.; Nagelkerke, A.; Belessiotis-Richards, A.; Payne, D. J.;

Gelmi, A.; Yarovsky, I.; Stevens, M. M. Surface Enhanced Raman Scattering Artificial Nose for High Dimensionality Fingerpriting. *Nat. Comm*un **2020**, *11*, 13615.

[92] Yan, B.; Hong, Y.; Chen, T.; Reinhard, B. M. Monitoring Enzymatic Degradation of Pericellular Matrices through SERS Stamping. *Nanoscale* **2012**, *4,* 3917-3925.

[93] van der Maaten, L.; Hinton, G. Visualizing Data Using t-SNE. *J Mach Learn Res* **2008**, *9*, 2579-2605.

[94] Lever, J.; Krzywinski, M.; Altman, N. Principal Component Analysis. *Nat. Methods* **2017**, *14*, 641-642.

[95] Ye, J.; Janardan, R.; Li, Q. Two-Dimensional Linear Discriminat Analysis. In *Advances in Neural Information Processing Systems* **2005**, *17*, 1569-1576.

[96] Chen, C.; Hsu, A. High Dimensional Data Visualization by PCA and LDA, Hsinchu, Taiwan: National Tsing Hua University. **2015**.

[97] Lee, J. S.; Wang, R. X.; Alexeev, E. E.; Lanis, J. M.; Battista, K. D.; Glover, L. E.; Colgan, S. P. Hypoxanthine Is A Checkpoint Stress Metabolite in Colonic Epithelial Energy Modulation And Barrier Function. *J. Biol. Chem.* **2017**, *293*, 6039-6051.

Supporting Information

Characterizing Nanoplastics-Induced Stress and Its SERS Fingerprint in an Intestinal Membrane Model

Qianyun Zhang and Björn M. Reinhard

Department of Chemistry and The Photonics Center, Boston University, Boston, Massachusetts, United States

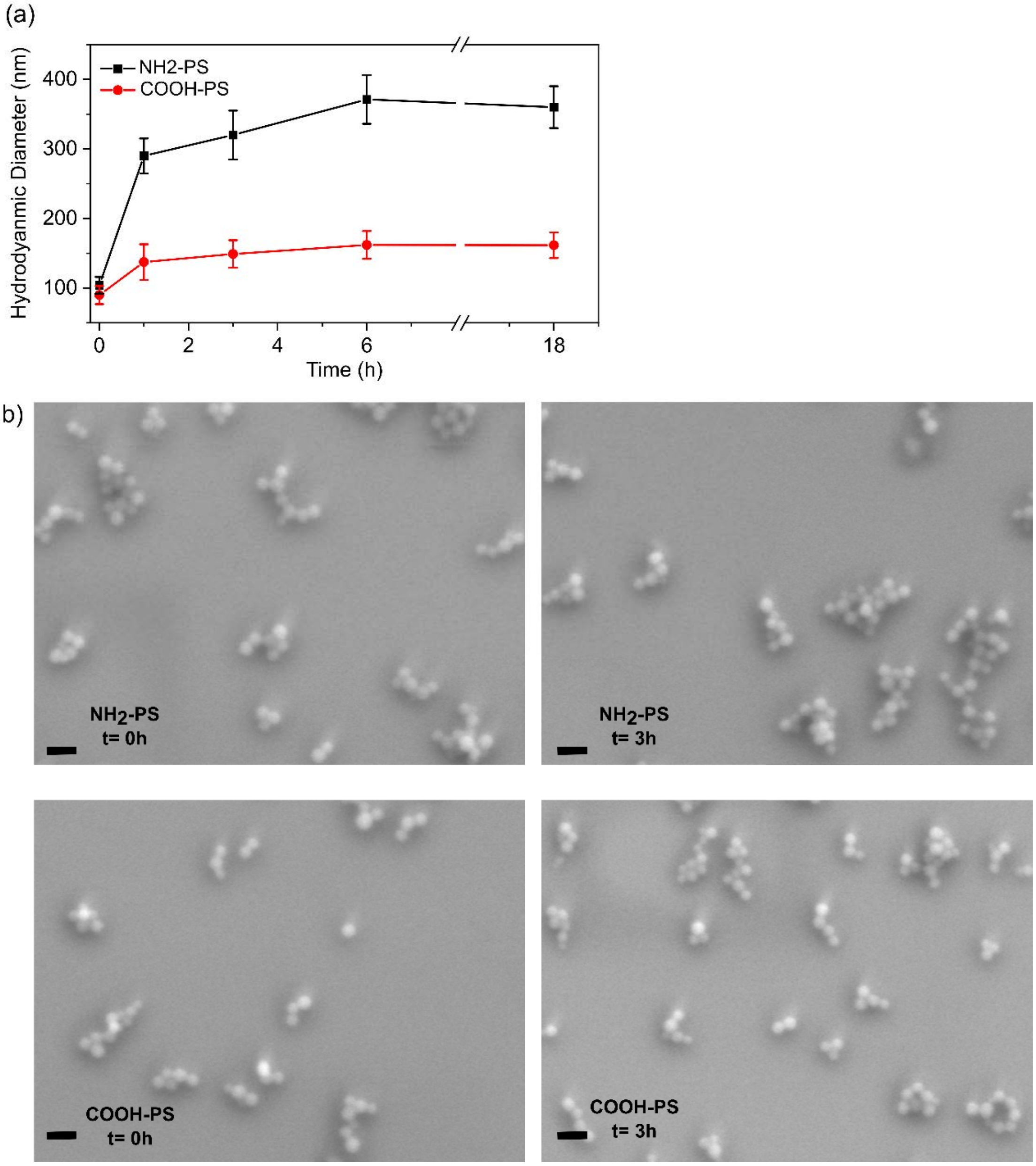

Figure S1: a) Hydrodynamic diameter of NH$_2$-PS and COOH-PS in growth medium as function of time. The hydrodynamic diameter of nanoparticles were measured at concentration of 1×10^{12} NP mL^{-1}. The reported results represent the mean of 3 independent experiments. b) SEM images of NH$_2$-PS and COOH-PS in growth medium for t= 0h and t= 3h. SEM samples were prepared by first coat the clean Si wafers with poly-L-Lysine. 50 µl of NH$_2$-PS and COOH-PS ($1\text{x}10^{12}$ NPs ml^{-1}) in growth medium were placed on the coated Si wafers, and incubate for 30 min at room temperature in a self-made humidity chamber. The excessive NPs solutions were then removed, and the wafers were washed with MQ water. Scale bar: 100 nm.

Table S1: Fluorescent dye release control experiments of two PS NPs. NH_2-PS (*C2*: 6x10^{12} NPs mL^{-1}) and COOH-PS (*C2:* 1x10^{14} NPs mL^{-1}) in DPBS (pH=7.4) were shaking for 18 h. The fluorescent intensity of PS NPs before shaking, after shaking, and supernatant were measured. DPBS was used as a blank control. The data in table represent an average of n=3 independent experiments. * indicates a significant difference from DPBS (control) at the $p<0.05$ level.

	COOH-PS FL Intensity [arb. unit]	**NH_2-PS FL Intensity [arb. unit]**
Before shaking	192391±1532*	79616±895*
After shaking	188117±2801*	74773±1055*
Supernatant	40.5±5.2	27.3±4.2
DPBS (control)	24.6±1.1	24.6±1.1

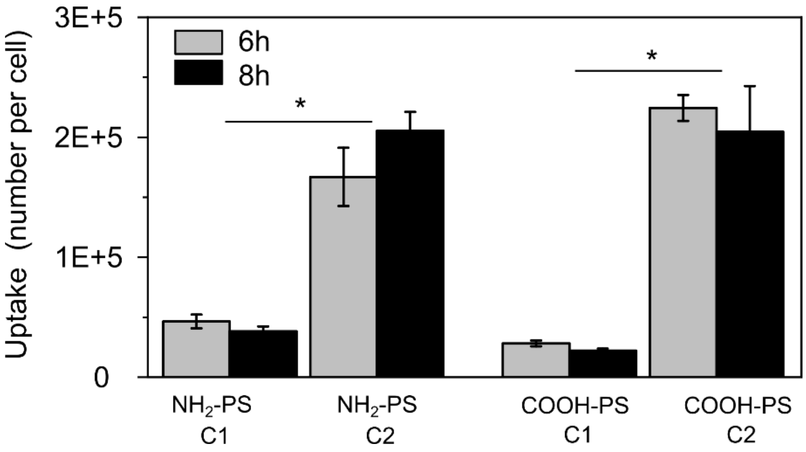

Figure S2: Particle uptake in the Caco-2 cell monolayer after incubation with NH_2-PS (*C1*: 1x10^{12} NPs mL^{-1} and *C2*: 6x10^{12} NPs mL^{-1}) and COOH-PS (*C1*: 6x10^{12} NPs mL^{-1} and *C2*: 1x10^{14} NPs mL^{-1}) for 6 and 18 h. $p<0.05$, n=20. The data in figure represent an average of n=20 independent experiments. * indicates a significant difference at the $p<0.05$ level.

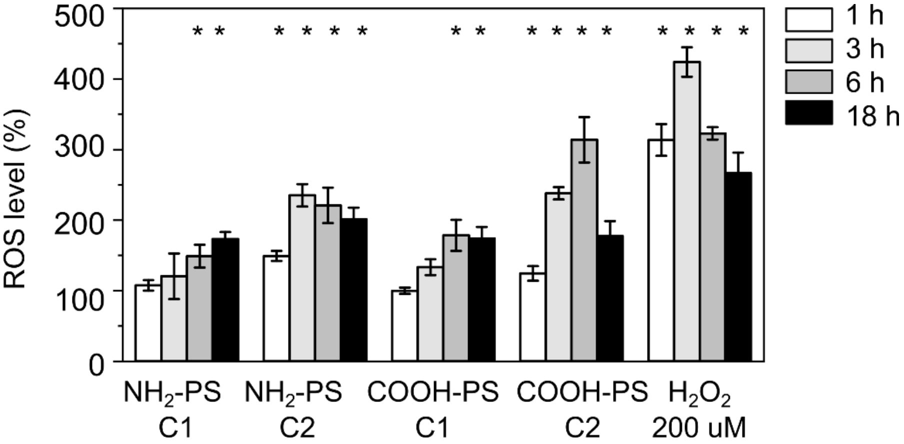

Figure S3: Characterization of ROS after incubation of monolayers of Caco-2 cell with NH_2-PS (*C1*: 1x10^{12} NPs mL^{-1} and *C2*: 6x10^{12} NPs mL^{-1}) and COOH-PS (*C1*: 6x10^{12} NPs mL^{-1} and *C2* 1x10^{14} NPs mL^{-1}) for 6 and 18 h. ROS indicator DCFH-DA intensity were normalized with cell numbers in each condition. Cell was stained with 0.2% trypan blue and cell number was counted with automated cell counter. The data was then normalized with the control group and are given in % (100% = control). H_2O_2 was included in as positive control. The data in figure represent an average of n=20 independent experiments. * indicates a significant difference at the $p<0.05$ level.

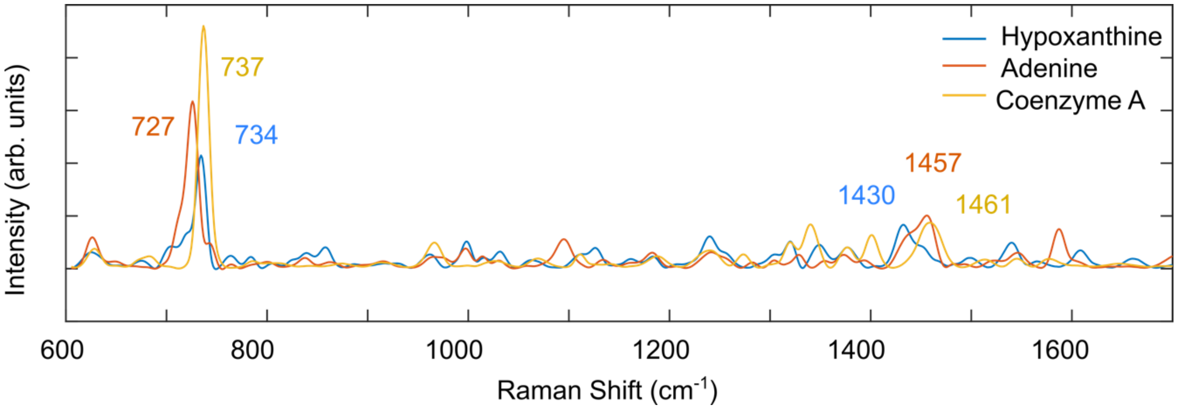

Figure S4: SERS spectrum of 1 μM of Coenzyme A, hypoxanthine and adenine in growth medium. SERS spectrum of each molecule in figure represent an average of 16 spectra. The predominant peak Raman shift of each molecule was labeled.

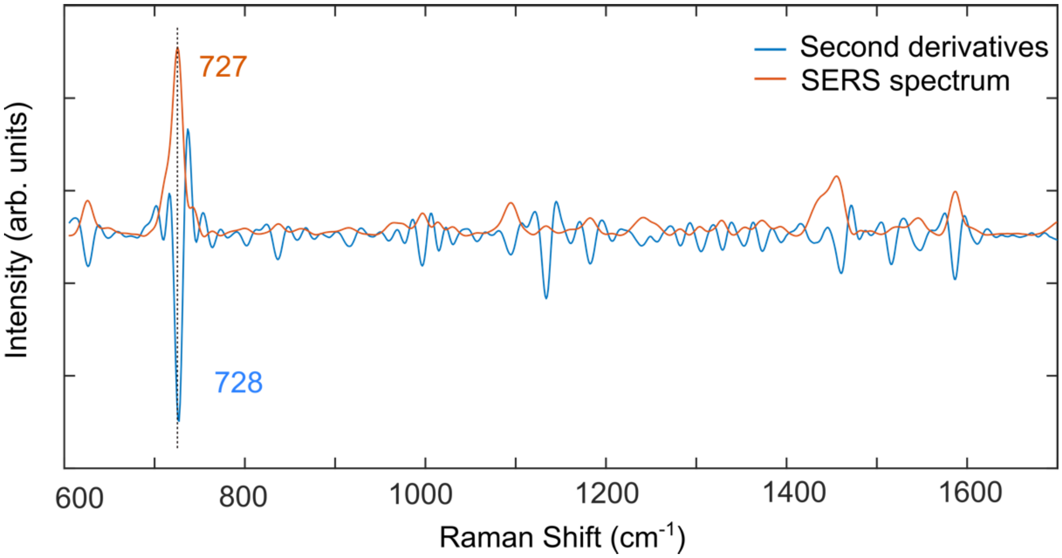

Figure S5: Comparison of the SERS spectrum of hypoxanthine (1x10^{-7} M) and the second derivatives. The discrimination between 727 cm^{-1} and 728 cm^{-1} is due to spectral resolution in the range of 1 cm^{-1}.

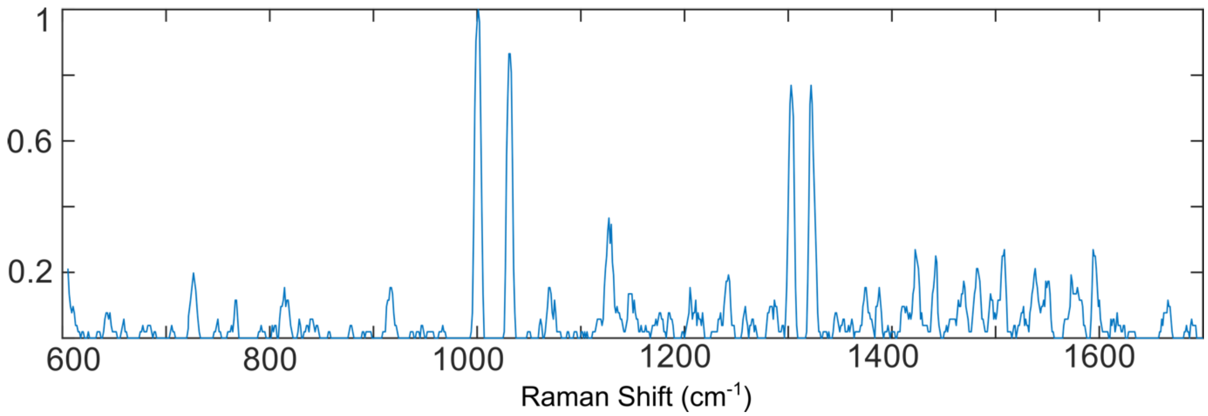

Figure S6: Histograms of the second derivative spectra collected from growth medium background. Data in the figure includes 25 SERS spectra.

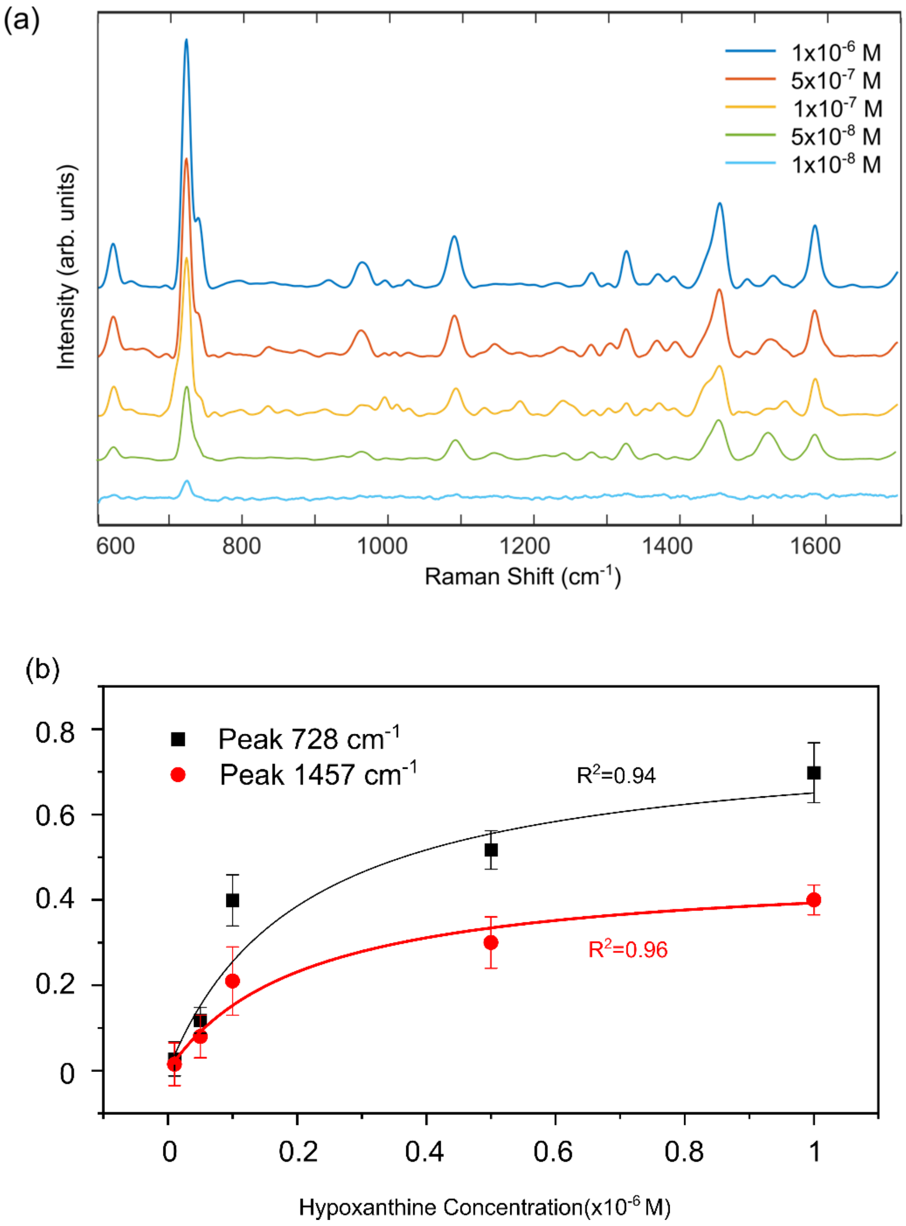

Figure S7: a) The SERS spectra of different concentration of hypoxanthine in growth medium. The detection limit of hypoxanthine is 10nM. SERS spectrum of each condition in figure represent an average of 16 spectra. b) Integrated area of the 728 cm^{-1} and 1457 cm^{-1} peak in the SERS spectra of hypoxanthine with varying concentration. The peak areas were determined by Lorentzian fits. Data obtained from 16 spectra and fitted with a sigmoidal curve.

Table S2: SERS band assignments for prominent peaks in PCA-LDA analysis

SERS peak [cm^{-1}]	Vibrational mode	Major Assignments
705	N-H bending	Proteins
712	C-N	Lipids DNA/RNA
728	C-H ring bending	Hypoxanthine
1002	C-H ring stretching	Phenylalanine
1032	C-H ring bending	Phenylalanine
1115	C-N stretching	Protein
1320	C-O stretching CH_2 twisting	Lipids Adenine DNA/RNA
1345	C-H stretching	Lipids
1457	C-N ring stretching CH_2 bending	Hypoxanthine
1547	C-C stretching	Protein
1610	C=O stretching	Amide I